This is a preprint, the final version is subject to change, of the American Mineralogist (MSA)
Cite as Authors (Year) Title. American Mineralogist, in press.
(DOI will not work until issue is live.) DOI: http://dx.doi.org/10.2138/am-2017-6009

Revision 3(Roger Mason revision):

Orientation of exsolution lamellae in mantle xenolith pyroxenes and implications for calculating exsolution pressures

Shan-Rong Zhao·, Ge-Ge Zhang, Hui Sun, Roger Mason, and Xu He

School of Earth Sciences, China University of Geosciences, Wuhan, 430074,

P. R. China

Abstract

Exsolution lamellae in pyroxene occurring in mantle lherzolite xenoliths in Cenozoic basalts from the Mingxi area, Fujian Province, China have been investigated by electron backscattered diffraction (EBSD) to determine epitaxial relationships between host and lamellae. Clinopyroxene (diopside) hosts developed two sets of lamellae: one of orthopyroxene (pigeonite-enstatite) lamellae and the other of clinopyroxene (augite) lamellae. Orthopyroxene (enstatite) hosts developed a single set of clinopyroxene (augite) lamellae. A zone crossing method has been used to determine Miller indices of lamellae which appear as linear traces on thin sections tested by EBSD. In clinopyroxene hosts, the index of orthopyroxene lamellae is (100) and that of clinopyroxene lamellae is ~(401) at 22° to the *c*-axis. In orthopyroxene hosts, the index of clinopyroxene lamellae is (100). Published high-pressure crystallographic data for compositions approximating those of the lamellae and host are used to compare cell parameters of lamellae and hosts at different pressures. Exact phase boundary theory is applied to estimate the exsolution pressure, and the data uncertainty of composition, cell parameters and orientation of the lamellae have been analyzed. Uncertainties of composition and cell parameters give rise to only small uncertainties in the exsolution pressure, but that of the orientation of the lamellae generates large uncertainty. Independent high accuracy measurement of the angle between lamellae and *c*-axis by TEM or other techniques combined with exact phase

· Corresponding author (email:shanrongzhao@126.com)

boundary theory would give more reliable estimates of exsolution pressure.

Key words: Exsolution, pyroxene, crystallographic orientation, mantle xenoliths, error-analysis, EBSD

Introduction

Exsolution microstructures are very common in pyroxene, e.g. clinohypersthene lamellae in augite and augite lamellae in pigeonite (Deer, Howie and Zussman, 2013; Champness and Lorimer, 1973), pigeonite and hypersthene lamellae in augite, augite lamellae in pigeonite and hyperthene (Bown and Gay, 1959), clinoenstatite lamellae in low-Ca orthopyroxene (Boland, 1974), low-Ca orthopyroxene lamellae in augite (Mikouchi and Miyamoto, 2008), enstatite lamellae in diopside and diopside-augite lamellae in enstatite-pigeonite (Zhu and Xu, 2007), magnetite in clinopyroxene (Fleet, et al., 1980; Feinberg et al., 2004). Most exsolution microstructures in minerals separate during cooling but in ultrahigh pressure (UHP) metamorphic rocks the exsolution structures more likely formed during decompression from more than 100 km depth to the surface. Exsolution lamellae of clinoenstatite in diopside found in UHP metamorphic rocks from the Alpe Arami massif, Switzerland (Bozhilov et al. 1999), and in UHP metamorphic rocks from the Dabie Mountains, China (Liu et al., 2007), suggest a minimum pressure of precipitation of ~ 12 Gpa for Alpe Arami and ~9 Gpa for Dabie Mountain (Liu et al., 2007) implying that the rocks were exhumed from a minimum depth of ~300 km. These exsolution structures might also have formed by shear strain during deformation rather than cooling and decompression (Kirby and Etheridge 1981, Coe and Muller 1973, Coe and Kirby 1975).

The relative crystallographic orientations of lamellae within hosts are critical for determining exact phase boundaries (Robinson et al., 1977) and calculation of exsolution temperatures and pressures based thereupon (Fleet et al., 1980; Feinberg et al., 2004). Electron backscattered diffraction (EBSD) enables rapid determination of crystallographic orientations within crystals exposed on the surfaces of polished thin sections, and is less cumbersome and not as labor intensive than TEM and

single-crystal XRD methods. Exsolution lamellae appear as linear traces on polished thin sections tested by EBSD but this requires a method to determine the crystallographic plane indices of the lamellae. We previously introduced a method called "zone crossing" to determine crystallographic plane indices of linear traces on thin sections (Zhao et al., 2016) that can be widely used to determine the plane indices of any kind of lamellae appearing as linear traces on thin sections tested by EBSD.

In this paper, we describe exsolution microstructures in clinopyroxene and orthopyroxene hosts in mantle lherzolite xenoliths in Cenozoic basalts from the Mingxi area, Fujian Province, China using this technique to determine the orientations of the lamellae within the hosts and the plane indices of the lamellae. The orientation of the lamellae combined with analysis of high-pressure crystallographic data for compositions approximating those of the lamellae and host permit us to estimate exsolution pressure using exact phase boundary theory. We have also carried out an analysis of data uncertainty to evaluate the application of exact phase boundary theory.

Sample description and experimental method

The pyroxene crystals studied occur in mantle lherzolite xenoliths in Cenozoic basalts from the Mingxi area, Fujian Province, China. The mineral assemblage of the lherzolite xenolith is: forsterite 80%, orthopyroxene 13%, clinopyroxene 6% and spinel 1%.

A lherzolite rock sample was sectioned and polished. The chemical composition of the pyroxene was measured by electron-microprobe analysis (EMPA) using a JEOL-JAX-8100 instrument at the State Key Laboratory of Geological Processes and Mineral Resources, China University of Geosciences. The samples were coated with a thin conductive carbon film prior to analysis using an accelerating voltage of 15 kV, a beam current of 20 nA and a 5 μm spot size. The chemical compositions of the lamellae and hosts are listed in Table 1.

A series of alpha alumina powers of decreasing grain size from 9μm to 0.5μm were used for surface grinding before the EBSD test, then a 0.3μm alpha alumina

solution and a 0.05μm colloidal silica solution were used for further polishing for more than 2h. Orientation analysis was carried out by the EBSD technique on a FEI Quanta 450 FEG environmental scanning electron microscope at the State Key Laboratory of Geological Processes and Mineral Resources, China University of Geosciences. Working conditions were as follows: 20 kV accelerating voltage, 6 spot size, 25 mm working distance, 70° sample tilt angle and partial vacuum 30 Pa, applied to an uncoated sample. Channel 5+ software from HKL technology, Oxford Instruments, was used to index the diffraction patterns. To ensure data quality, only those measurements with mean angular deviation (MAD) values below 1° were accepted for analyses. The accuracy of the poles on pole figure is below 1°.

The cell parameters of the pyroxene were measured by X-ray powder diffraction using a Bruker AXS D8-Focus diffractometer and Cu Kα radiation operated at 40kV and 40mA. During analysis, the samples for XRD were measures from 5° to 80° (2θ) with a step size of 0.02° (2θ) and a counting time of 0.2s per step. Cell parameters calculated by the least square method were: *C*2/*c*, a=9.694(2)Å, b=8.862(2)Å, c=5.258(2)Å, β=106(1) for clinopyroxene hosts; *Pbca*, a=18.230(5)Å, b=8.804(2)Å, c=5.185(2)Å, β=90 for orthopyroxene hosts.

Results

Fig. 1 shows SEM images and pole figures of three clinopyroxene host crystals and their exsolution lamellae. There are two sets of lamellae in each clinopyroxene host. We obtained backscattered Kikuchi diffraction patterns at several points in the hosts and the lamellae, indicated as 1, 2, 3…on the images. The Kikuchi diffraction patterns confirm that the hosts are clinopyroxene. One set of lamellae has diffraction patterns consistent with orthopyroxene, and the other set of lamellae has the same Kikuchi diffraction pattern as the host. Because the lamellae are very thin, we tested many points across them to confirm that the test points on the hosts and lamellae, have the same Kikuchi diffraction patterns. This confirmed that the other set of lamellae is clinopyroxene.

Fig. 2 shows SEM images and pole figures of two orthopyroxene host crystals

and their lamellae. There is only one set of lamellae in each orthopyroxene host crystal. Kikuchi diffraction patterns confirm that the host is orthopyroxene and the lamellae are clinopyroxene.

Data from the EBSD system used to digitize and analyze the diffraction patterns were: a=9.794Å, b=8.906Å, c=5.319Å, β=105.9 for clinopyroxene (Peacor, 1967); a=18.320Å, b=8.917Å, c=5.219Å for orthopyroxene (Domeneghetti et al., 1996).

Fig.1

Fig.2

The compositions of the hosts and lamellae were determined by electron microprobe analysis (EMPA). An analyzed clinopyroxene host is diopside, one of its lamellae is pigeonite-enstatite and the other is augite; an orthopyroxene host is enstatite and its lamella is augite (see Table 1). Compositions determined by EMPA are indicated in Figs. 1 and 2.

Table 1

Analysis and discussion

Determination of the crystallographic planes of the lamellae

The crystallographic orientations of exsolution lamellae in pyroxene hosts are critical for estimating exsolution temperatures and pressures by the exact phase boundary method. The lamellae appear as linear traces on thin sections. We have introduced a “zone crossing” method to determine the Miller indices of lamellae appearing as linear traces on thin sections (Zhao, et al., 2016) and used this method to determine the crystallographic planes of the lamellae in this paper.

The main idea of this “zone crossing” method is: A linear trace is intersected by many planes which belong to a zone. The same lamella appears as different linear traces on different crystal sections with different orientation. These linear traces represent different zones. These zones must cross at a point, which is the pole of the crystallographic plane corresponding to the lamellae. We used this zone crossing method to determine the crystallographic plane index of the lamellae.

We combined the <100>, <010> and <001> poles of one crystal as shown in

Figs. 3 and 4 which make it clear that the orientation relationship between orthopyroxene lamellae and clinopyroxene host or orthopyroxene host and clinopyroxen lamellae is that <001> and <010> coincide but <100> has a 16° deviation. This angle is the difference between β angles of the ortho- and clino-pyroxenes. The Kikuchi diffraction pattern of clinopyroxene (augite) lamellae is the same as their clinopyroxene (diopside) host, and therefore the crystallographic orientation between the clinopyoxene host and clinopyroxene lamellae is the same.

We plotted the traces of lamellae on the pole figures shown in Figs. 3 and 4. A linear trace is intersected by many planes which belong to a zone, and the poles of these planes in the zone distribute on the upright line of the linear trace. We plotted upright lines of the traces on the pole figures in Figs. 3 and 4, and the pole of the lamella plane must be on its upright line. We drew 9~10 points on the upright lines, which we used to transform these upright lines into great circles, as the coordination transformed.

Fig. 3

Fig. 4

Then we transformed the coordination of the pyroxene hosts into a general orientation for orthopyroxene: <100> at coordinate (φ = 90°, ρ = 90°), <010> at (φ = 0°, ρ = 90°) and <001> at (ρ = 0°); and for clinopyroxene: <100> at (φ = 270°, ρ = 180° - β), <010> at (φ = 0°, ρ = 90°) and <001> at (ρ = 0°). The upright lines were transformed into great circles shown in Figs. 5 and 6 using a Wulff net.

Fig. 5

Fig. 6

Finally we overlapped the pole figures for Crystals 1, 2 and 3 with clinopyroxene hosts and Crystals 4 and 5 with orthopyroxene hosts, to find the cross points of the zones shown in Fig. 7.

Fig. 7

In Fig. 7, the zones representing clinopyroxene lamellae in clinopyroxene hosts (Crystals 1, 2 and 3) cross at point A and the zones representing orthopyroxene lamellae in the clinopyroxene hosts (Crystals 1, 2 and 3) cross at point B. The zones

representing clinopyroxene lamellae in orthopyroxene hosts (Crystals 4 and 5) cross at point C. Points B and C have coordinates ($\varphi = 90°$, $\rho = 90°$), and are determined by the plane Miller index of the orthopyroxene lamellae in clinopyroxene hosts and clinopyroxene lamellae in orthopyroxene hosts is (100). The angle between point A and the pole of (100) is 22°. The plane index of clinopyroxene lamellae in the clinopyroxene host is ~(401).

Previous publications state that orthopyroxene lamellae in clinopyroxene hosts or clinopyroxene lamellae in orthopyroxene hosts are always (100) (Robinson, et al.,1977; Champness and Lorimer, 1973; Kirby and Etheridge 1981). This is due to the fact that the (100) plane has a similar atomic arrangement in clino- and orthopyroxenes. The epitaxial relationship between these two phases is: <001> and <010> coincide but <100> has a 16° deviation (the difference between the β angles of ortho- and clinopyroxenes). The index of clinopyroxene lamellae in clinopyroxene hosts is ~(401) and depends on the exsolution temperature or/and pressure, according to the exact phase boundary. We will discuss the exsolution pressure later.

This demonstrates that the zone crossing method is very useful to determining the crystallographic plane index of a lamella appearing as a linear trace on a section tested by EBSD. Any kinds of planes in a crystal, such as exsolution lamellae, composition planes and interfaces, must appear as linear traces on the sections. If there are two or more linear traces in differently orientated sections, and these traces belong to the same plane, the zone crossing method can be used to determine the crystallographic index of this plane.

Exsolution pressure of the ~(401) lamellae determined by exact phase boundary theory

The optimal phase boundary theory was first introduced by Robinson et al. (1971) and Jaffe et al. (1975), and later clarified and refined for pyroxene exsolution as exact phase boundary theory by Robinson et al. (1977). This theory aims to find a geometric fit between lamellae and host lattices that minimizes interface energy. This best fit varies as the lattice parameters of the lamellae and host change with temperature or/and pressure.

In this theory the two monoclinic phases, which have identical *b*-dimensions and similar structure are intergrown so that their (010) planes are parallel. An *exact phase boundary* between the two phases lies a plane oriented parallel to the common *b*-direction and which contains a vector *Y* directed parallel to the common (010) plane. The magnitude of the unit-repeat of vector *Y* in terms of the phase 1 and phase 2 unit-cell parameters is given by

$$|Y|_1=(a_1^2x_1^2+c_1^2z_1^2+2a_1c_1\cos\beta_1x_1z_1)^{1/2} \quad \text{for phase 1} \quad \text{----------(1)}$$

$$|Y|_2=(a_2^2x_2^2+c_2^2z_2^2+2a_2c_2\cos\beta_2x_2z_2)^{1/2} \quad \text{for phase 2} \quad \text{----------(2)}$$

where *x* and *z* are coordinates of the vector *Y* in the *a* and *c* directions, respectively, and *a*,*c* and β are the unit-cell parameters at the temperature and pressure of initial phase separation. To provide an *exact phase boundary*, vectors Y_1 and Y_2 must be equal in magnitude:

$$|Y|_1= |Y|_2 \quad \text{----------(3)}$$

Fig. 8 shows a sketch of boundary orientations between augite lamellae and diopside host. This boundary has an angle of 22° from the *c* direction because the index of the boundary is ~(401). The vector *Y* is shown in Fig.8.

Fig. 8

This boundary orientation varies as the cell parameters of the lamellae and host change with temperature and/or pressure and therefore the boundary orientation is a fossil indicator of lattice parameters at high temperature and/or pressure and hence can be used as geothermometers or geobarometers (Robinson et al., 1977). Because the mantle lherzolite xenoliths crystallized under high pressure and the exsolution lamellae are probably formed during decompression from upper mantle depths to the surface, we here consider the pressure effect and ignore the temperature effect.

Tribaudino et al. (2000) reported the cell parameters Di_{100} and $Di_{80}En_{20}$ at different pressures. We plot the cell parameters *a*, *c* and β vs. pressure for Di_{100} and $Di_{80}En_{20}$ in Fig. 9. Then we measured the cell parameters Di_{100} and $Di_{80}En_{20}$ at 1, 2, 3, 4, 5, 6, 7, 8 and 9 Gpa on the plot, and list them in Table 2. The composition of our sample is Di_{98} (host) and Di_{54} (lamellae) [Di = 2×Wo = 2×Ca/ (Ca+Mg+Fe+Mn), see Table 1]. We calculated the cell parameters of our sample with interpolation by

equation (4).

$$a = a(Di_{100}) - [a(Di_{100}) - a(Di_{80})]\, Q/20 \text{ ----------(4)}$$

Here a or c or β are the cell parameters Di_{98} or Di_{54} and $a(Di_{100})$ and $a(Di_{80})$ are the cell parameters Di_{100} and Di_{80}, respectively. Q = 100-98 = 2 for Di_{98} and Q = 100-54 = 46 for Di_{54}. We list these cell parameters of our sample in Table 3 and plot them in Fig. 9.

Fig. 9

Table 2

Table 3

From Fig. 8 we know that if z =1, x can be calculated by

$$x = c \sin 22° / a \sin (180°-22°- \beta) \text{ ----------(5)}$$

We calculate a series of values of x with different cell parameters at different pressures for the diopside host (Di_{98}) and augite lamellae (Di_{54}) according to equation (5), and calculate a series of values of Y for the diopside host (Di_{98}) and augite lamellae (Di_{54}) according to equations (1) or (2). All of the calculated data are listed in Table 4.

Table 4

Because the vector Y is directed toward the *acute* β between the -a and + c directions, x should have a negative value when calculating Y by equation (1) or (2).

From Table 4 we find that the difference between vector Y(host) and Y' (lamellae) achieves a minimum at the pressure 4 GPa and therefore we suggest that the exsolution pressure of the ~(401) lamellae at 22° to the c axis in the diopside host is ~4 Gpa.

Evaluation of data quality by considering the uncertainty of the data.

There are three kinds of uncertainty of data which need to be considered.

1) uncertainty of composition: the EMPA measurement errors could generate ±1 uncertainty for Di_{98} (host) and Di_{54} (lamellae);

2) uncertainty of cell parameters: the cell parameters of Di_{100} and $Di_{80}En_{20}$ reported by Tribaudino et al. (2000) have an average uncertainty of 0.0005Å and the measurement of the cell parameters of Di_{100} and $Di_{80}En_{20}$ at 1, 2, 3, 4, 5, 6, 7, 8 and 9

Gpa on the plot in Fig. 9 could generate another uncertainty. We suggest that the uncertainty of cell parameters is 0.001Å;

3) uncertainty of the angle between the lamellae and *c* axis: EBSD measurement could generate an uncertainty below 1°. We suggest that the uncertainty of the angle is 0.5°.

We calculated a series of uncertainties for *x* generated by the three kinds of uncertainties described above and list them in Tables 5, 6 and 7.

Tables 5, 6 and 7.

We calculated the uncertainty of cell parameters generated by Di±1 first, then calculated the uncertainty of *x* generated by Di±1. All these data are listed in Table 5 which shows that the uncertainty of *x* generated by Di±1 is 0.00003-0.00005 for Di_{98} and Di_{54}. Table 6 lists the uncertainty of *x* generated by the 0.001Å uncertainty of cell parameters of Di_{100} and $Di_{80}En_{20}$ and shows that the uncertainty of *x* generated by this 0.001Å uncertainty of cell parameters is 0.00005 for Di_{98} and 0.00015 for Di_{54}. Table 7 lists the uncertainty of *x* generated by ± 0.5° of the angle between the lamellae and *c* axis and shows that the uncertainty of *x* generated by this ± 0.5° is 0.0058 for Di_{98} and Di_{54}. This uncertainty of ± 0.0058 is much greater than the uncertainty of *x* generated by the uncertainties of composition and cell-parameter, showing that the orientation of the lamellae (the angle between the lamellae and *c* axis) is the most important factor influencing the uncertainty of *x*, and thus the uncertainty of exsolution pressure.

We can estimate the uncertainty of the exsolution pressure from Table 4 based on the uncertainties of *x*. The uncertainties ± 0.00003, ± 0.00005 and ±0.00015 of *x* generated by the uncertainties of composition and cell parameter correspond to an uncertainty of < 0.5 Gpa in pressure, and the uncertainty of ± 0.0058 of *x* generated by the uncertainty of the orientation of the lamellae corresponds to an uncertainty of ~ 4 Gpa in pressure! This large uncertainty means that the range of exsolution pressure is comparable to the estimated pressure itself.

The error-analysis discussed above indicates that the application of exact phase boundary theory for estimating pressure or temperature is highly dependent on the accuracy of the measurement of the angle between the lamellae and *c* axis. Even a

very small error of the angle could generate a large error for pressure or temperature. An EBSD test cannot determine this angle accurately enough. It must be tested by TEM or other techniques that have higher accuracy. By contrast, errors of measurements of composition and cell parameters generate a small error for the pressure or temperature.

The exact phase boundary theory has been reported for quite a long time. The application of this theory is a complex procedure that involves various parameters and the data uncertainty has not been analyzed before. In this paper we have analyzed different kinds of data uncertainties and compared their importance for the exsolution pressure.

Although there is a large uncertainty, the method proposed in this paper to determine the exsolution pressure is a new and simple way to apply exact phase boundary theory and is simpler than that reported by Liu et al. (2007). In their paper, high pressure clinoenstatite (HPclen) exsolution lamellae in an augite host was determined from ultrahigh pressure rocks in the Dabie Mountains UHP terrain, and the orientation of the lamellae was ~(401). The authors used the exact phase boundary theory reported by Robinson et al. (1977) in the equation

$$(a^2_1 - a^2_2)\, x^2 + (2a_1c_1\cos\beta_1 - 2a_2c_2\cos\beta_2)\, x + (c^2_1 - c^2_2) = 0 \qquad \text{----------(5)}$$

to calculate maximum and minimum values of the cell parameters of the host augite, when the lamellae orientation was (401). In equation (5), a_1, c_1, β_1 and a_2, c_2, β_2 are cell parameters of host and lamellae, respectively. The cell parameters of HPclen lamellae were obtained from high pressure crystallographic data for HPclen and HPpig (Shinmei et al. 1999; Nestola et al. 2004), and the x = 1/4, when they used equation (5) who determined the area of the maximum and minimum values of the cell parameters of the host augite vs. pressure to show possible cell parameters of the host augite when generating the (401) lamellae. Based on the cell parameter vs. pressure plot for Di_{100} and $Di_{80}En_{20}$ (Tribaudino et al. 2000), a plot of cell parameter vs. pressure for the augite host was obtained by interpolation according to compositions of Di_{100} and $Di_{80}En_{20}$. When the plot of cell parameter vs. pressure for augite host enters the area of the maximum and minimum values of the cell

parameters of the host augite vs. pressure, the cross point of the plot and the area determined the minimum value of the exsolution pressure. This calculation procedure was described in the Deposit item AM-07-008 Appendix of their paper (Liu et al. 2007). The minimum exsolution pressure for HPclen lamellae in augite host in Dabie Mountain area is 9GPa based on this method.

This calculation procedure to determine the exsolution pressure for HPclen lamellae in augite host described above was very complex, and the resultant exsolution pressure cannot be an exact value. In this paper, we have proposed a different way to apply exact phase boundary theory to estimate exsolution pressure and have tried to find a minimum of the difference between *Y*(host) and *Y*'(lamellae), such that the corresponding pressure should be the exsolution pressure. This is simpler than the method reported by Liu et al. (2007).

Implications

There are several geobarometers applicable to mantle rocks, e.g. the garnet-orthopyroxene geobarometer (Nickel and Green, 1985; Taylor, 1998; Brey et al., 2008), garnet-clinopyroxene geobarometer (Nimis and Taylor, 2000; Simakov and Taylor, 2000), olivine-clinopyroxene geobarometer (Finnerty and Boyd, 1978; Finnerty and Rigden, 1981), Cr-in spinel geobarometer (O`Neill, 1981) and two-pyroxene geobarometer (Hersberg, 1978; Gasparik, 1984; Mercier et al., 1984). After discussing the precision and the accuracy of these geobarometers, Wu (2009) proposed that only the garnet-orthopyroxene and garnet-clinopyroxene geobarometers are relatively valid, and the others are obviously far from accurate and precise. That is geobarometers for mantle rocks are limited.

All these geobarometers are based on chemical equilibrium experiments. The errors of experimental data, deviations of the experimental chemical systems from actual rock chemical systems, etc., decrease the precision and the accuracy of these geobarometers. The exact phase boundary theory of Robinson et al. (1977) presents a different kind of geobarometer based on the geometric fit between lamellae and host lattices that minimizes interface energy and is a beneficial supplement to

geobarometers based on the chemical equilibrium experiments and calculations. However this geobarometer involves 7 parameters: the lattice parameters of the lamellae and host (a, c, β and a', c', β'), and the orientation of the lamellae in the host (x). These parameters make the application of this theory complicated and it is necessary to find a way to simplify the application of this theory. In this paper, we have introduced a way to simplify. However, our data uncertainty analysis of exact phase boundary theory shows that the exsolution pressure is highly dependent on the accuracy of the measurement of the angle between the lamellae and the c axis. The angle between lamellae and c axis should be measured carefully with high accuracy by TEM or other techniques for exact phase boundary theory to be applied to estimate exsolution pressure.

Although EBSD cannot provide a high accurate measurement of the angle between lamellae and c axis at present, it is an efficient technique for rapidly determining crystallographic orientations of crystals, and is less cumbersome and not as labor intensive compared to TEM and single-crystal XRD methods. Exsolution lamellae appear as linear traces on thin sections tested by EBSD and it is necessary to find a method to determine the crystallographic Miller indices of exsolution lamellae. In this paper, we have used a method called zone crossing to determine the Miller indices of exsolution lamellae on thin sections. This zone crossing method can be widely used to determine the indices of any kind of lamellae appearing as linear traces on the thin sections tested by EBSD.

Acknowledgments

We are grateful to Dr Xiang-Wen Liu for the discussion about the application of the exact phase boundary theory, to Dr Xin-Rong Lei for the discussion about the date uncertainty analysis. We acknowledge financial support from National Nature Science Fundation of China (41372058). The EBSD was performed in State Key Laboratory of Geological Processes and Mineral Resources, China University of Geosciences.

References cited

Boland, J.N. (1974) Lamellar structures in low-calcium orthopyroxenes. Contributions to Mineralogy and Petrology, 47, 215-222

Bown, M.G., and Gay, P. (1959) The identification of oriented inclusions in pyroxene crystals, American Mineralogist, 44, 592-602

Bozhilov, K.N., Green, H.W.II, Dobrzhinetskaya, L.F. (1999) Clinoenstatite in Alpe Arami peridotite: Additional evidence of very high pressure. Science, 284, 128-132

Brey, G.P., Bulatov, V.K., and Gimis, A.V. (2008) Geobarometry for peridotites: Experiments in simple and natural system from 6 to 10 GPa. Journal of Petrology, 49, 3-24

Champness, P.E., Lorimer, G.W. (1973) Precipitation (exsolution) in an orthopyroxene. Journal of of Material Science, 8, 467-474

Coe, R.S., Kirby, S.H. (1975) The orthoenstatite to clinoenstatite transformation by shearing and reversion by annealing: Mechanism and potential applications. Contributions to Mineralogy and Petrology, 52, 29-55

Coe, R.S., Muller, W.F. (1973) Crystallographic orientation of clinoenstatite produced by deformation of orthoenstatite: Science, 180, 64-66

Deer, W.A., Howie, R.A., and Zussman, J. (2013) Introduction to the Rock-Forming Minerals (Third Edition): Mineralogical Society London, 498pp.

Domeneghetti, M.C., Tazzoli, V., Boffa, B.T. et al. (1996) Orthopyroxene from the Serra de Mage meteorite: A structure refinement procedure for a *Pbca* phase coexisiting with a *C*2/*c* exsolved phase. American Mineralogist, 81, 842-846

Feinberg, J.M., Wenk, H.R., Renne, P.R., Scott, G.R. (2004) Epitaxial relationships of clinopyroxene-hosted magnetite determined using electron backscatter diffraction (EBSD) technique. American Mineralogist, 89, 462-466

Finnerty, A.A., and Boyd, F.R .(1978) Pressure-dependent solubility of Ca in forsterite coexisting with diopside and enstatite. Carnegie Institution of

Washington Yearbook, 77, 713-717

Finnerty, A.A., and Rigden, S.M. (1981) Olivine barmetry: Application to pressure estimation for terrestrial and lunar rocks. Lunar and Planetary Science, XII, 279-281

Fleet, M.E., Bilcox, G.A., Barnett, R.L. (1980) Oriented magnetite inclusions in pyroxene from the Grenville Province. Canadian Mineralogist, 18, 89-99

Gasparik, T. (1984) Two-pyroxene thermobarometry with new experimental data in the system CaO-MgO-Al_2O_3-SiO_2. Contributions to Mineralogy and Petrology, 87, 87-97

Hersberg, C.T. (1978) Pyroxene geothermometry and geobarometry: Experimental and thermodynamic evaluation of some subsolidus phase relations involving pyroxenes in the system CaO-MgO-Al_2O_3-SiO_2. Geochimica et Cosmochimica Acta, 42, 945-957

Jaffe, H.W., Robinson, P.,Tracy, R.J., Ross, M. (1975)Orientation of pigeonite lamellae in metamorphic augite: correlation with composition and calculated optimal phase boundaries. American Mineralogist, 60, 9-28

Kirby, S.H., and Etheridge, M.A. (1981) Exsolution of Ca-clinopyroxene from orthopyroxene aided by deformation. Physics and Chemistry of Minerals, 7, 105-109

Liu, X.W., Jin, Z.M., Green, H.W.II. (2007) Clinopyroxene exsolution in diopsidic augite of Dabieshan: Garnet peridotite from depth of 300 km. American Mineralogist, 92, 546-552

Mercier, J.C.C., Benoit, V., and Girardeau, J. (1984) Equilibrium state of diopside-bearing harzburgites from ophiolites: Geobarmetric and geodynamic implications. Contributions to Mineralogy and Petrology, 85, 391-403

Mikouchi, T., and Miyamoto, M. (2008) Mineralogy and pyroxene cooling rate of unique achondritic meteorite GRA 06129. Lunar and Planetary Science XXXIX, 2297.pdf

Nestola, F., Tribaudino, M., Ballaran, T.B. (2004) High Pressure behavior, transformation and crystal structure of synthetic iron-free pigeonite. American

Mineralogist, 89, 189-196

Nickel, K.G., and Green, D.H. (1985) Empirical geothermobarometry for garnet peridotites and implication for the nature of the lithosphere, kimberlites and diamonds. Earth and Planetary Science Letters, 73,158-170

Nimis, P., and Taylor, W.R. (2000) Single clinopyroxene thermobarometry for garnet peridotites. Part I. Calibration and testing of a Cr-in-Cpx barometer and an enstatite-in-Cpx thermometer, Contributions to Mineralogy and petrology, 139, 541-554

O`Neill, H.St.C. (1981) The transition between spinel lherzolite and garnet lherzolite, and its use as a Geobarometer. Contributions to Mineralogy and Petrology, 77, 185-194

Peacor, D.R.(1967) Refinement of the crystal structure of pyroxene of formula $M_1M_2(Si_{1.5}Al_{0.5})O_6$. American Mineralogist, 52, 31-41

Robinson, P., Ross, M., Nord, GL-Jr., Smyth, J.R., Jaffe, H.W. (1977) Exsolution lamellae in augite and pigeonite: fossil indicators of Iattice parameters at high temperature and pressure. American Mineralogist, 62, 857-873

Robinson, P., Jaffe, H.W., Ross, M. and Klein, Jr. C. (1971) Orientation of exsolution lamellae in clinopyroxene and clinoamphiboles: consideration of optimal phase boundaries. American Mineralogist, 56, 909-939

Shinmei, T., Tomioka, N., Fujino, K., Kuroda, K., Irifune, T. (1999) In situ X-ray diffraction study of enstatite up to 12 GPa and 1473 K and equations of state. American Mineralogist, 84, 1588-1594

Simakov, S.K., and Taylor, L.A. (2000) Geobarometry for mantle eclogites: Solubility of Ca-tschermaks in clinopyroxene. International Geology Review, 42, 534-544

Taylor, W.R. (1998) An experimental test of some geothermometer and geobarometer formulations for upper mantle peridotites with application to the thermobarometry of fertile lherzolite and garnet websterite. Neues Jahrbuch fur Mineralogie Ahhandlungeu, 172, 381-408

Tribaudino, M., Prencipe, M., Bruno, M., et al.(2000) High-pressure behaviour of

Ca-rich C2/c clinopyroxenes along the join diopside-enstatite ($CaMgSi_2O_6$-$Mg_2Si_2O_6$). Physics and Chemistry of Minerals, 27, 656-664

Wu., C. M.(2009) On the validity of the geobarometers in mantle rocks. Acta Petrologica Sinica, 2089-22112(in Chinese)

Zhao, S.R., Xu, C., Xu, H.J., Zhang, B.M., Liu, H.F.(2016) Crystallographic orientation of exsolution microstructure in pyroxene, occurring in iherzolite from Wenchang area, Hainan, China. Acta Petrologica Sinica, 32(6), 1644-1652(in Chinese)

Zhu, Y.F., and Xu, X. (2007) Exsolution texture of two-pyroxenes in iherzolite from Baijiantan ophiolitic mélange, western Junggar, China. Acta Petrologica Sinica, 23(5), 1075-1086(in Chinese)

Figure captions

(a) (b)

Fig. 1 (a) SEM images of the three clinopyroxene hosts (Crystals 1, 2 and 3) and their lamellae; (b) Pole figures of Crystals 1, 2 and 3 and their lamellae

(a) (b)

Fig. 2 (a) SEM images of the two orthopyroxene hosts (Crystals 4 and 5) and their lamellae; (b) Pole figures of Crystals 4 and 5 and their lamellae

Fig. 3 The combination pole figures of the clinopyroxene hosts (Crystals 1, 2 and 3) and their lamellae, displaying the lamelale traces and their upright lines

Fig. 4 The combination pole figures of the orthopyroxene hosts (Crystals 4 and 5) and their lamellae, displaying the lamelale traces and their upright lines

Fig. 5 Pole figures of the clinopyroxene hosts with the general orientation, displaying the zones containing their lamellae

Fig. 6 Pole figures of the orthopyroxene hosts with the general orientation, displaying the zones containing their lamellae

Fig. 7 (a) Zone cross points among the clinopyroxene hosts (Crystals 1, 2, and 3) (b) Zone cross points between the orthopyroxene hosts(Crystals 4 and 5)

Fig. 8 Sketch of boundary orientation between lamellae and host

Fig. 9 Cell parameter vs. pressure plot for Di_{100} and $Di_{80}En_{20}$ (Tribaudino et al. 2000), as well as that for augtite lamellae (Di_{54}) and diopside host (Di_{98}) in this paper

Tables

Table 1 Chemical compositions of the pyroxene hosts and their lamellae (EMPA)

	SiO_2	TiO_2	Al_2O_3	FeO	MnO	MgO	CaO	Na_2O	Cr_2O_3	totle
Cpx-host	52.848	0.181	6.479	2.332	0.078	14.277	20.988	1.744	0.860	99.785
	$(Ca_{0.813}\ Na_{0.122}\ Mg_{0.060})_{0.995}\ (Mg_{0.710}\ Al_{0.187}\ Fe_{0.071}\ Cr_{0.025}\ Ti_{0.005}Mn_{0.002})_{1.000}[(Si_{1.911}\ Al_{0.089})_{2.000}O_6]$									
	$Wo_{0.4911}En_{0.4663}Fs_{0.0426}$ (Di)									
Cpx-lamellae in Cpx host										
	54.032	0.122	5.534	4.139	0.093	21.778	12.601	1.052	0.662	100.010
	$(Ca_{0.478}\ Mg_{0.444}\ Na_{0.072})_{0.955}\ (Mg_{0.706}\ Al_{0.146}\ Fe_{0.123}\ Cr_{0.019}\ Mn_{0.003}Ti_{0.003})_{1.000}[(Si_{1.915}Al_{0.085})_{2.000}O_6]$									
	$Wo_{0.2727}En_{0.6574}Fs_{0.0699}$ (Aug)									
Opx-lamellae in Cpx host										
	55.886	0.030	4.478	6.009	0.116	29.769	3.781	0.310	0.360	100.733
	$(Mg_{0.826}\ Ca_{0.140}\ Na_{0.021})_{0.987}\ (Mg_{0.704}\ Fe_{0.173}\ Al_{0.109}\ Cr_{0.010}$									

$Mn_{0.003}Ti_{0.001})_{1.000}[(Si_{1.927}Al_{0.073})_{2.000}O_6]$

$En_{83}Fs_9Wo_8$ (En-Pig)

Opx-host	55.756	0.041	4.266	6.586	0.124	32.577	0.484	0.033	0.336	100.201

$(Mg_{0.969}Ca_{0.018}Na_{0.002})_{0.989}(Mg_{0.703}Fe_{0.190}Al_{0.093}Cr_{0.009}Mn_{0.004}Ti_{0.001})_{1.000}[(Si_{1.920}Al_{0.080})_{2.000}O_6]$

$En_{89}Fs_{10}Wo_1$ (En)

Cpx-lamellae in Opx host

54.237	0.181	5.066	4.422	0.104	23.663	11.219	0.820	0.570	100.281

$(Mg_{0.519}Ca_{0.424}Na_{0.056})_{0.999}(Mg_{0.724}Fe_{0.130}Al_{0.122}Cr_{0.016}Ti_{0.005}Mn_{0.003})_{1.000}[(Si_{1.911}Al_{0.089})_{2.000}O_6]$

$En_{69}Wo_{24}Fs_7$ (Aug)

Table 2 Cell parameters of the Di_{100} and Di_{80} measured on the plot in Fig. 9

P	Di_{100}			Di_{80}		
(GPa)	*a*(Å)	*c*(Å)	*β*(°)	*a*(Å)	*c*(Å)	*β*(°)
1	9.718	5.234	105.79	9.703	5.233	106.13
2	9.688	5.218	105.67	9.673	5.214	105.93
3	9.661	5.203	105.56	9.648	5.197	105.76
4	9.644	5.192	105.44	9.627	5.184	105.65
5	9.624	5.182	105.37	9.600	5.167	105.49
6	9.599	5.168	105.29	9.581	5.154	105.35
7	9.577	5.154	105.21	9.562	5.143	105.23
8	9.558	5.144	105.17	9.543	5.133	105.13
9	9.540	5.135	105.13	9.523	5.122	105.06

Table 3 Cell parameters of the diopsie host(Di_{98}) and augtite lamellae(Di_{54})

P	Host (Di_{98})			Lamellae (Di_{54})		
(GPa)	*a*(Å)	*c*(Å)	*β*(°)	*a′*(Å)	*c′*(Å)	*β′*(°)
1	9.7165	5.2339	105.824	9.6835	5.2317	106.572
2	9.6865	5.2176	105.696	9.6535	5.2088	106.268
3	9.6597	5.2024	105.580	9.6311	5.1892	106.020
4	9.6423	5.1912	105.461	9.6049	5.1736	105.923
5	9.6216	5.1805	105.382	9.5688	5.1475	105.646
6	9.5972	5.1666	105.296	9.5576	5.1358	105.428
7	9.5755	5.1529	105.212	9.5425	5.1287	105.256
8	9.5565	5.1429	105.166	9.5235	5.1187	105.078

9	9.5383	5.1337	105.123	9.5009	5.1051	104.969

Table 4 x and Y at different pressures for host(Di_{98}) and lamellae (Di_{54})

P(GPa)	Host (Di_{98})		Lamellae (Di_{98})		Y-Y'(Å)
	x	Y(Å)	x'	Y'(Å)	
1	0.25546	6.37494	0.25887	6.41369	0.03875
2	0.25501	6.34810	0.25745	6.36875	0.02065
3	0.25457	6.32332	0.25620	6.33118	0.00787
4	0.25408	6.30328	0.25579	6.30687	0.00359
5	0.25383	6.28605	0.25451	6.26013	-0.02592
6	0.25351	6.26459	0.25348	6.23426	-0.03033
7	0.25312	6.24351	0.25295	6.21651	-0.02699
8	0.25298	6.22895	0.25237	6.19501	-0.03394
9	0.25287	6.21554	0.25194	6.17284	-0.04270

Table 5 The uncertainty of cell parameters and x generated by Di±1

P (GPa)	Uncertainty of cell parameters Di_{98} and Di_{54}			Uncertainty of sin (180-β)		Uncertainty of x	
	δa(Å)	δc(Å)	δβ(°)	Di_{98}	Di_{54}	Di_{98}	Di_{54}
1	0.00075	0.00005	0.01700	0.000081	0.000085	0.000029	0.000031
2	0.00075	0.00020	0.01300	0.000061	0.000064	0.000027	0.000028
3	0.00065	0.00030	0.01000	0.000047	0.000048	0.000026	0.000026
4	0.00085	0.00040	0.01050	0.000049	0.000050	0.000032	0.000033
5	0.00120	0.00075	0.00600	0.000028	0.000028	0.000049	0.000049
6	0.00090	0.00070	0.00300	0.000014	0.000014	0.000042	0.000042
7	0.00075	0.00055	0.00100	0.000005	0.000005	0.000034	0.000034
8	0.00075	0.00055	0.00200	0.000009	0.000009	0.000034	0.000033
9	0.00085	0.00065	0.00350	0.000016	0.000016	0.000039	0.000039

(1) Uncertainty of cell parameters generated by Di±1: δa (or δc or $\delta\beta$) = $\{[a(Di_{100})-a(Di_{80})]^2 \times (1/20)^2\}^{1/2}$

[Based on equation (4)]

(2) Uncertainty of sin (180-β) generated by Di±1= [sin (180-β+$\delta\beta$)-in (180-β-$\delta\beta$)]/2

(3) Uncertainty of x generated by Di±1 = $x \times \{(\delta a/a)^2+(\delta c/c)^2 +[\text{uncertainty of sin}(180-\beta)/\sin(180-\beta)]^2)]^{1/2}$

[Based on equation (5)]

Table 6 The uncertainty of x generated by the 0.001 uncertainty of cell

parameters of Di_{100} and Di_{80}

	Uncertainty of sin (180-β)		Uncertainty of x	
P(GPa)	Di_{98}	Di_{54}	Di_{98}	Di_{54}
1	0.0000043	0.0000132	0.0000502	0.0001486
2	0.0000043	0.0000129	0.0000503	0.0001484
3	0.0000042	0.0000127	0.0000503	0.0001482
4	0.0000042	0.0000127	0.0000503	0.0001484
5	0.0000042	0.0000124	0.0000504	0.0001484
6	0.0000042	0.0000123	0.0000505	0.0001481
7	0.0000041	0.0000121	0.0000505	0.0001480
8	0.0000041	0.0000120	0.0000506	0.0001479
9	0.0000041	0.0000119	0.0000507	0.0001480

(1) Uncertainty of cell parameters: δa (or δc or $\delta\beta$) for Di_{98} = $\{[1-(100-98)/20)]^2\times0.001^2+[(100-98)/20]^2\times0.001^2\}^{1/2}$ = 0.00091 [Based on equation (4)]

(2) Uncertainty of cell parameters: δa (or δc or $\delta\beta$) for Di_{54} = $\{[1-(100-54)/20)]^2\times0.001^2+[(100-54)/20]^2\times0.001^2\}^{1/2}$ = 0.00264 [Based on equation (4)]

(3) Uncertainty of sin (180°-β) = [sin (180°-β+$\delta\beta$)-in (180°-β-$\delta\beta$)]/2, here $\delta\beta$ = 0.00091 and 0.00264 for Di_{98} and Di_{54}, respectively.

(4) Uncertainty of x generated by the 0.001 uncertainty of cell parameters of Di_{100} and Di_{80} = $x \times \{(\delta a/a)^2+(\delta c/c)^2+[\text{uncertainty of sin（180°-}\beta\text{)/sin（180°-}\beta\text{）}]^2)\}^{1/2}$, here δa (or δc) = 0.00091 and 0.00264 for Di_{98} and Di_{54}, respectively. [Based on equation (5)]

Table 7 The uncertainty of x generated by ± 0.5° of the angle between (401) lamellae and c axis.

	Uncertainty of x (Å)	
P(GPa)	Di_{98}	Di_{54}
1	0.005773	0.005850
2	0.005763	0.005818
3	0.005753	0.005790
4	0.005742	0.005781
5	0.005736	0.005752
6	0.005729	0.005728
7	0.005720	0.005716
8	0.005717	0.005703
9	0.005715	0.005693

(1) Uncertainty of sin 22° generated by ± 0.5°: $\delta\theta$ = (sin 22.5° - sin 21.5°)/2 = 0.00809

(2) Uncertainty of sin (180°-β -22°) generated by ± 0.5°: $\delta\theta'$ = [sin (180°-β -22.5°) - sin (180°-β -21.5°)]/2 = 0.005289. To simplify, β here takes the average value 105.3°

(3) Uncertainty of x generated by ±0.5° of the angle between lamellae and c axis = $x \times \{(\delta\theta / \sin 22°)^2 + [\delta\theta' / \sin(180° - \beta - 22°)]^2\}^{1/2} = x \times 0.022588$, here $\beta = 105.3°$ [Based on equation (5)]

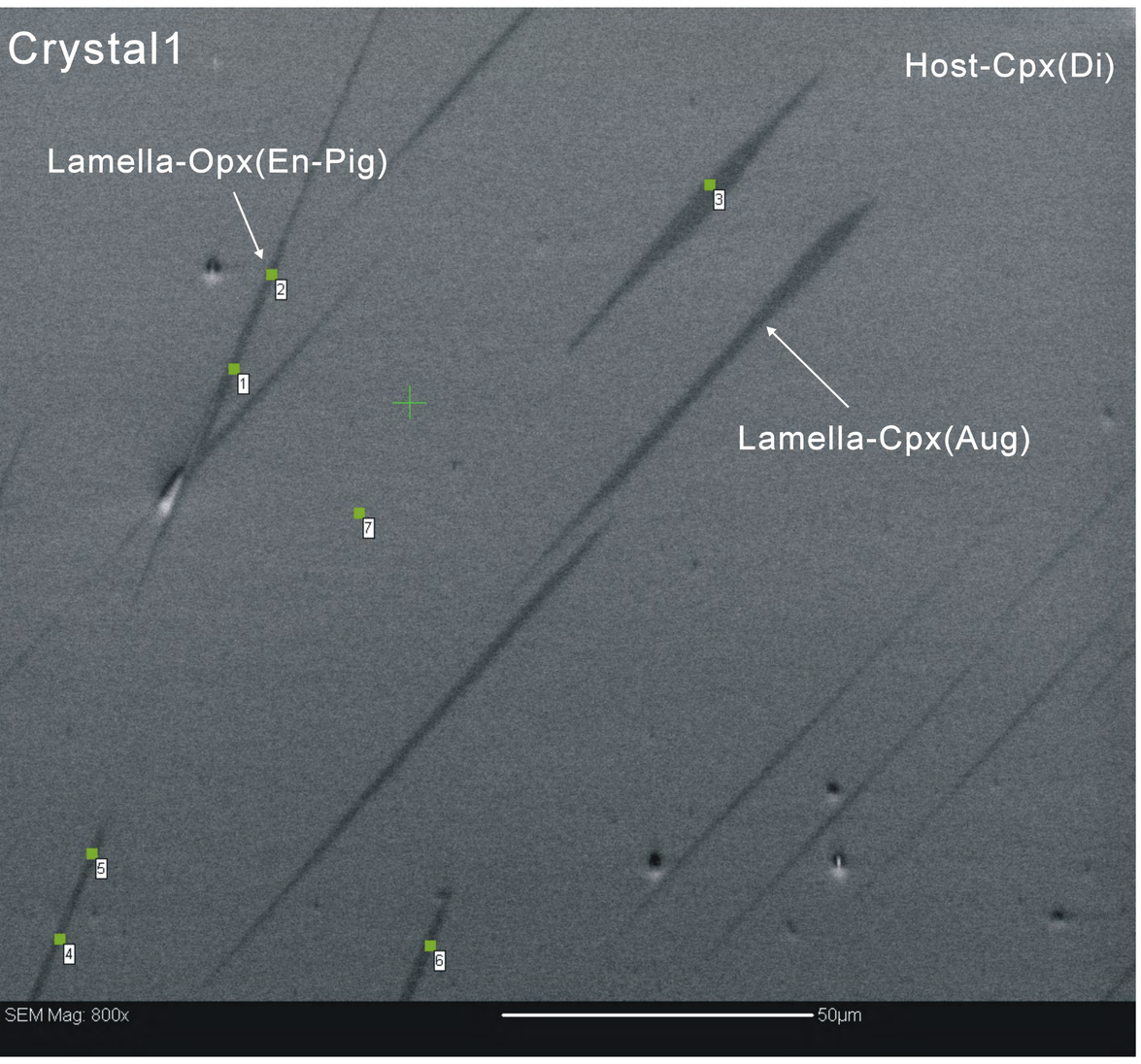

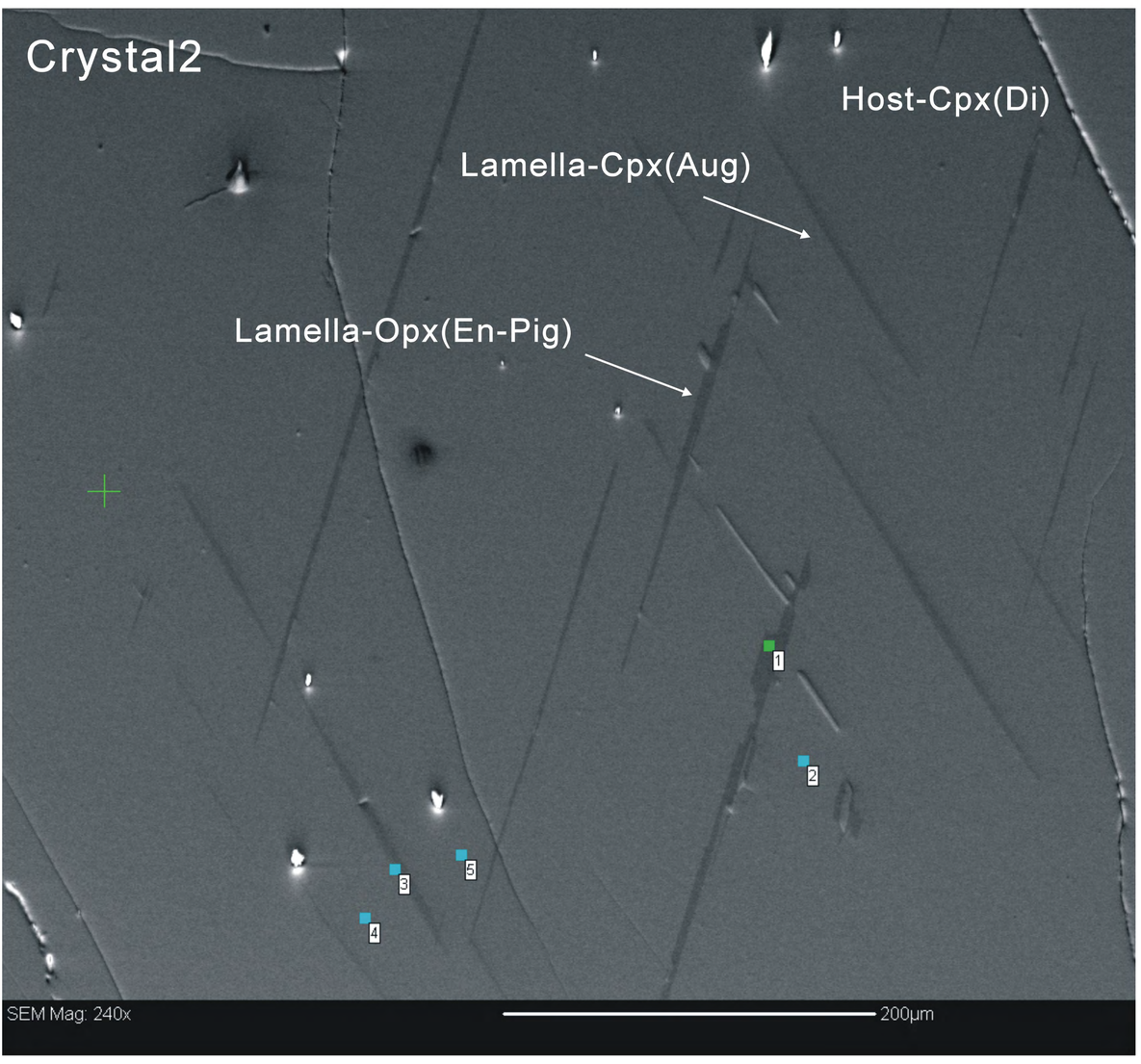

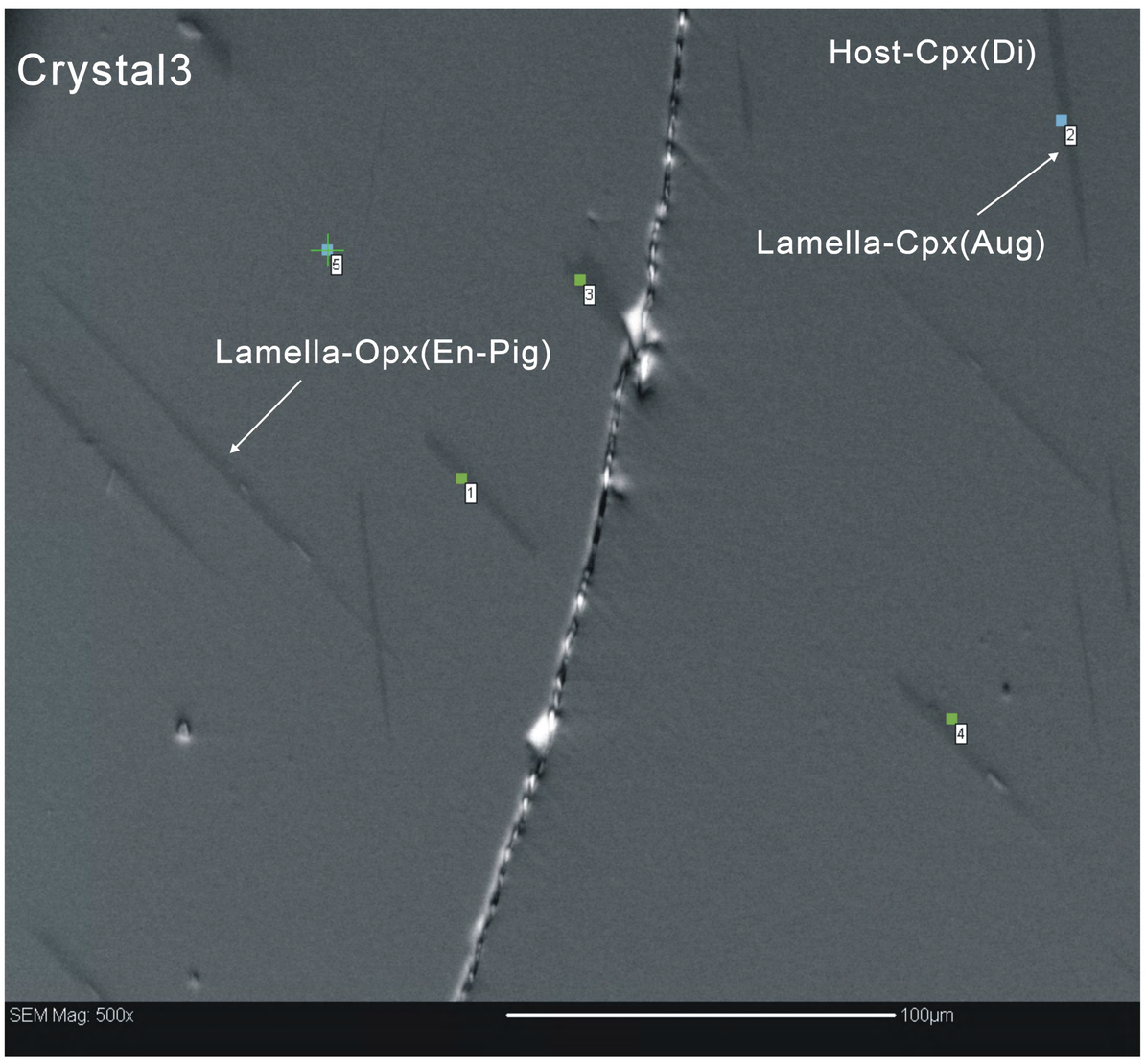

(a)

Crystal1-Cpx host and Cpx lamellae

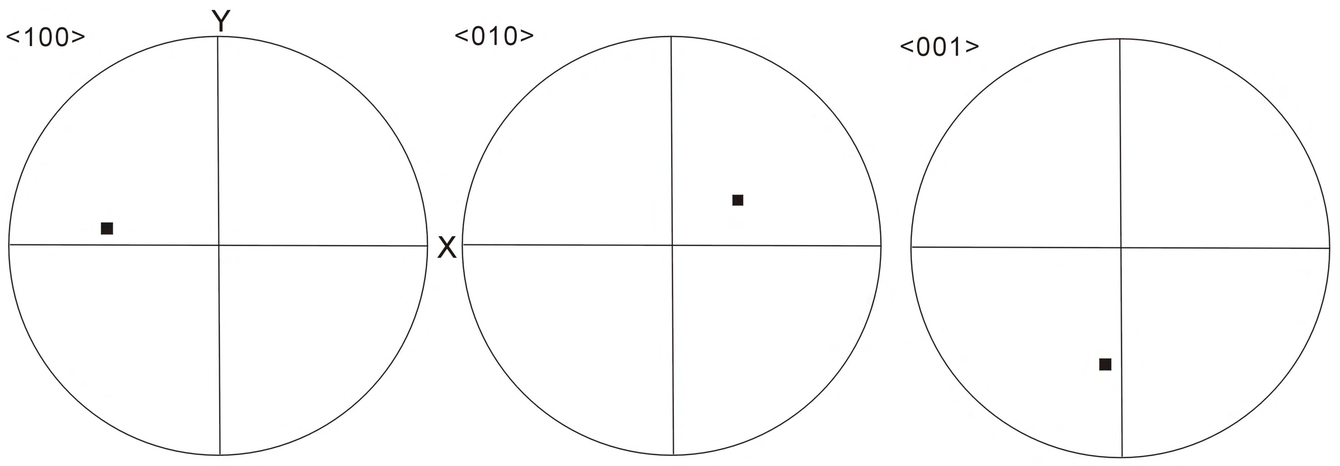

Crystal1-Opx lamellae

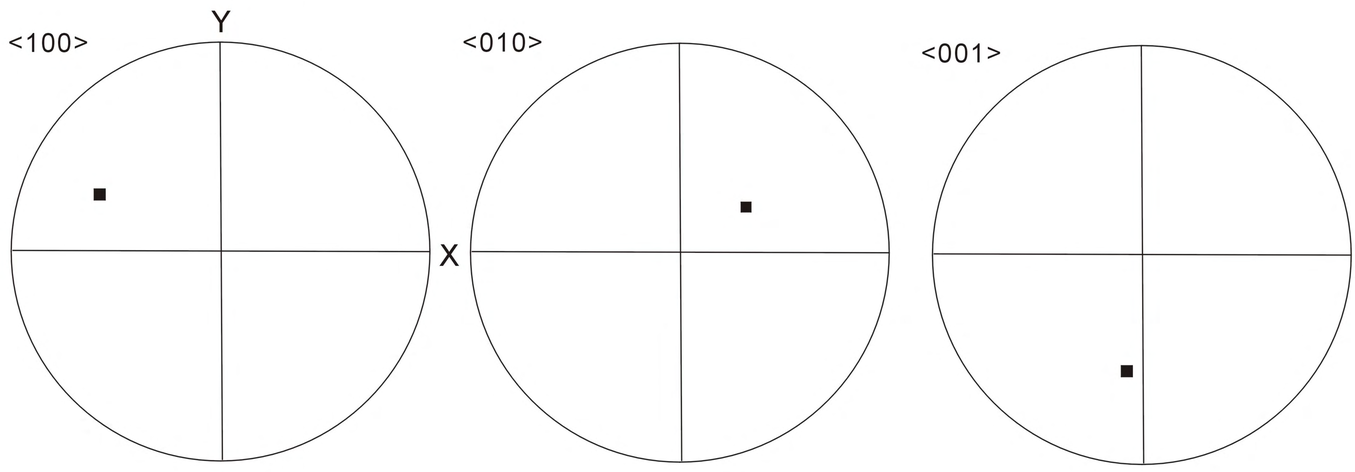

Crystal2-Cpx host and Cpx lamellae

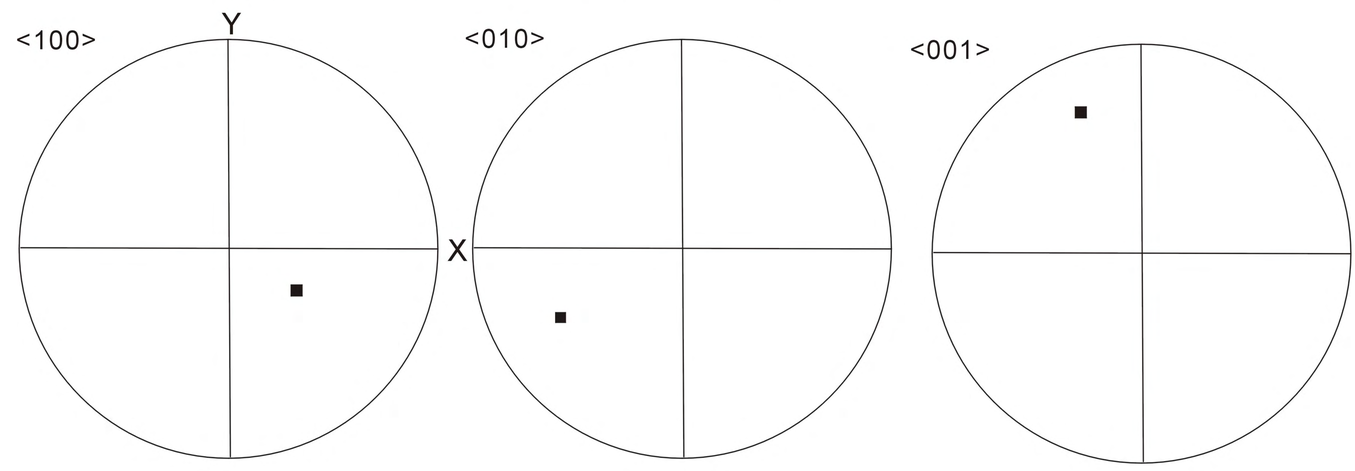

Crystal2-Opx lamellae

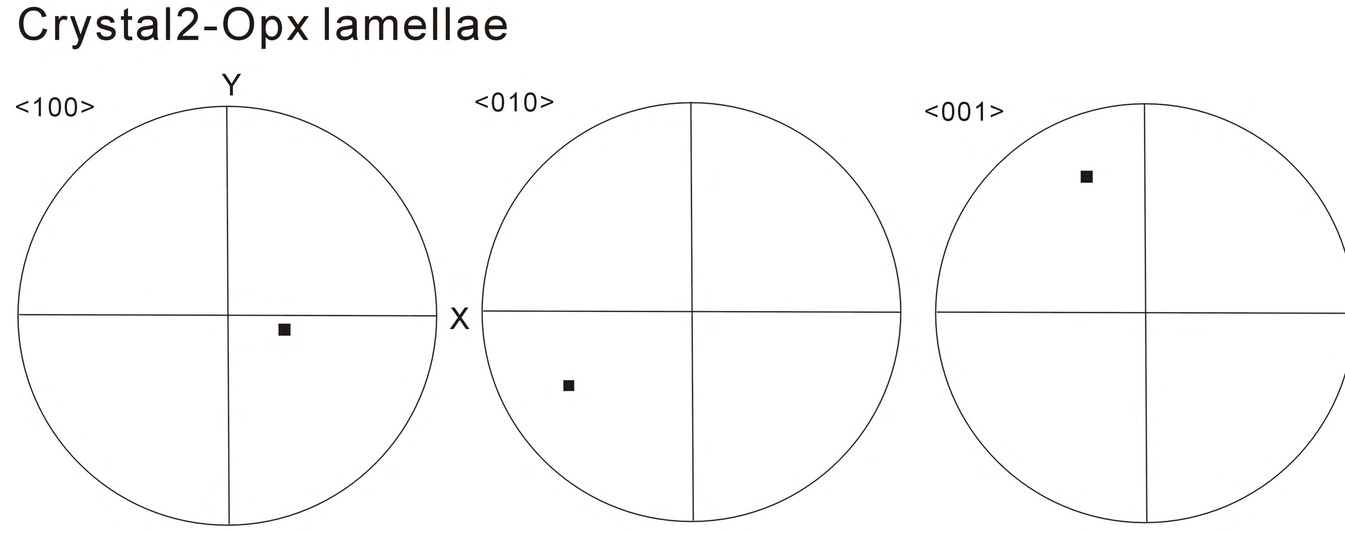

Crystal3-Cpx host and Cpx lamellae

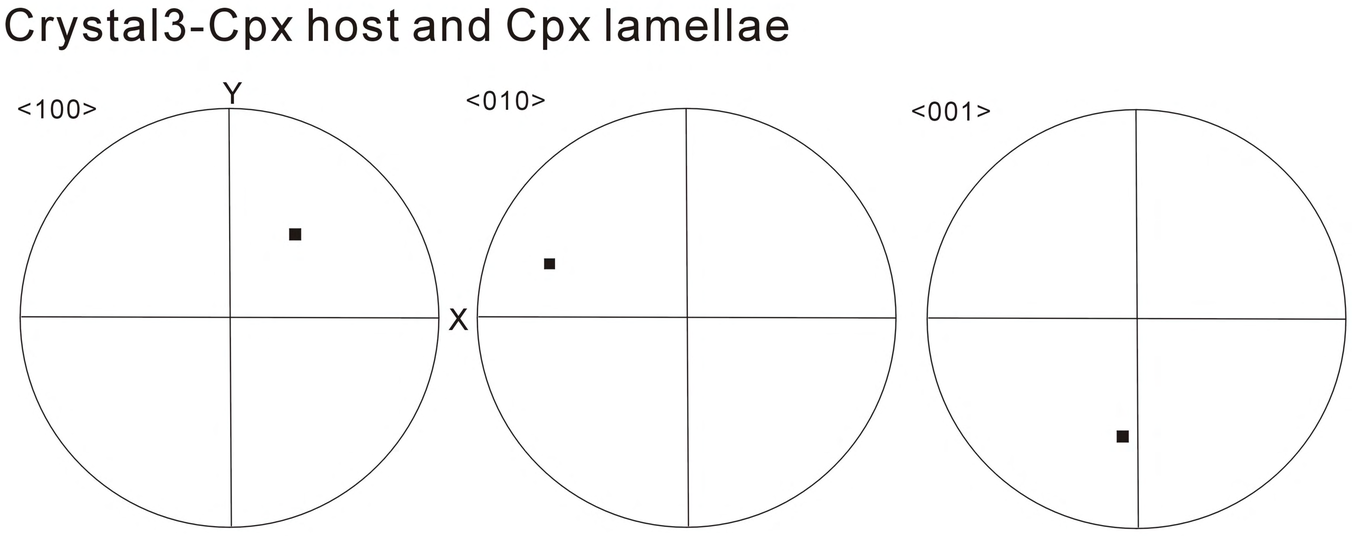

Crystal3-Opx lamellae

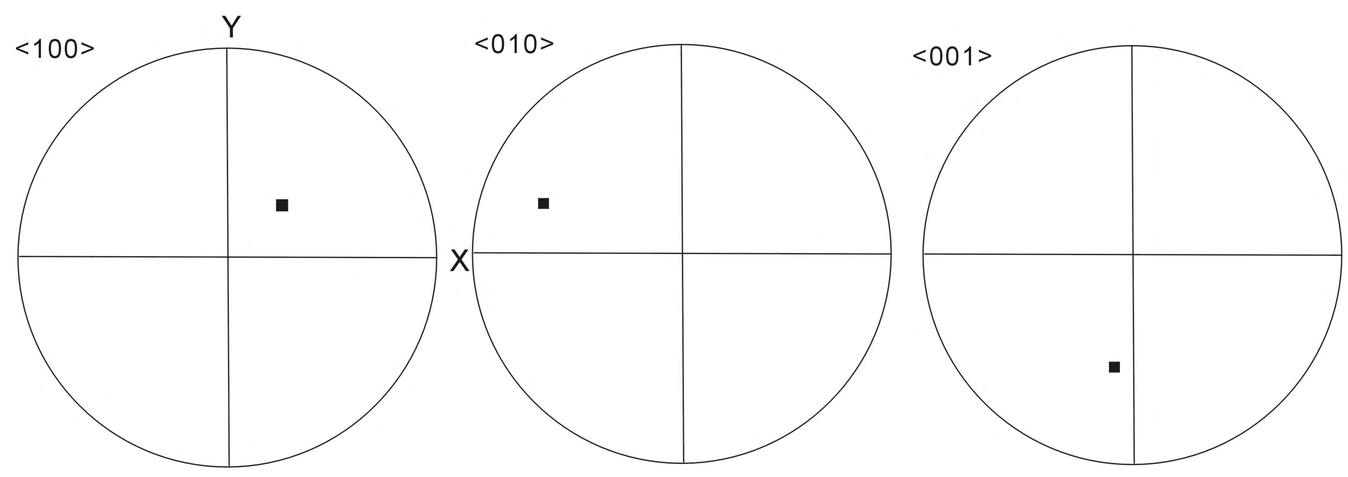

(b)

Figure 1

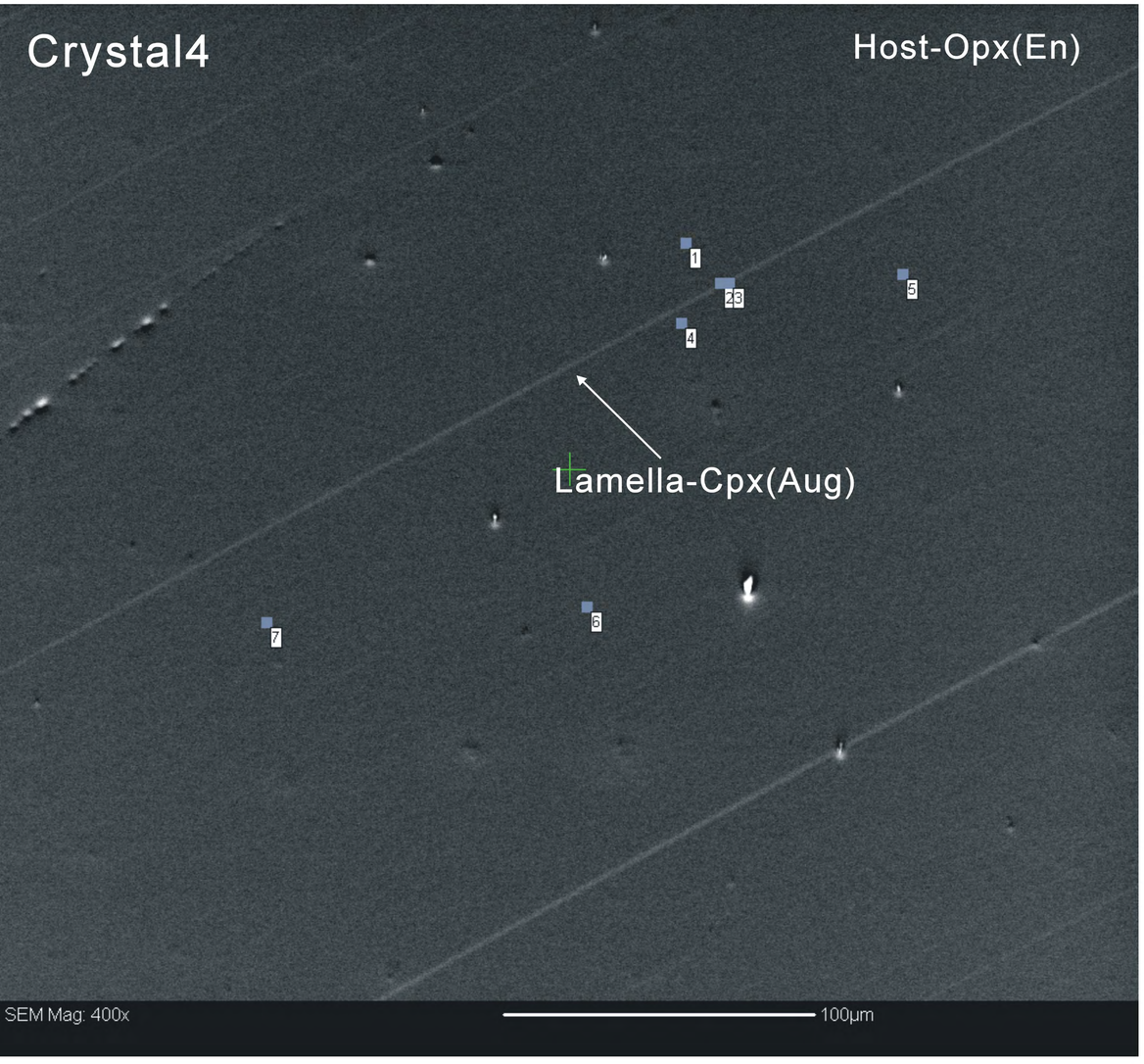
Crystal4
Host-Opx(En)
Lamella-Cpx(Aug)
1
2
3
4
5
6
7
SEM Mag: 400x
100μm

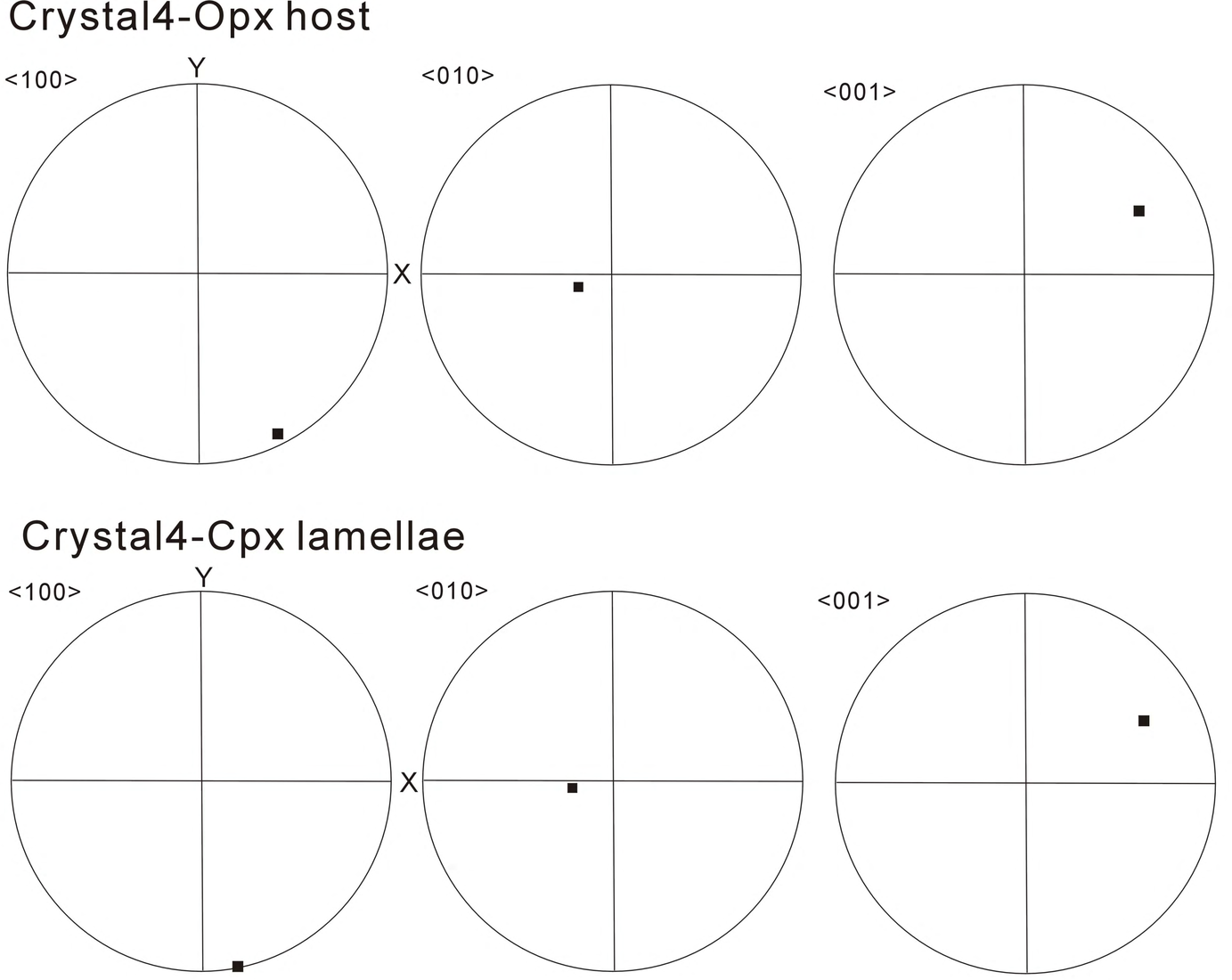
Crystal4-Opx host
<100>
Y
X
<010>
<001>
Crystal4-Cpx lamellae
<100>
Y
X
<010>
<001>

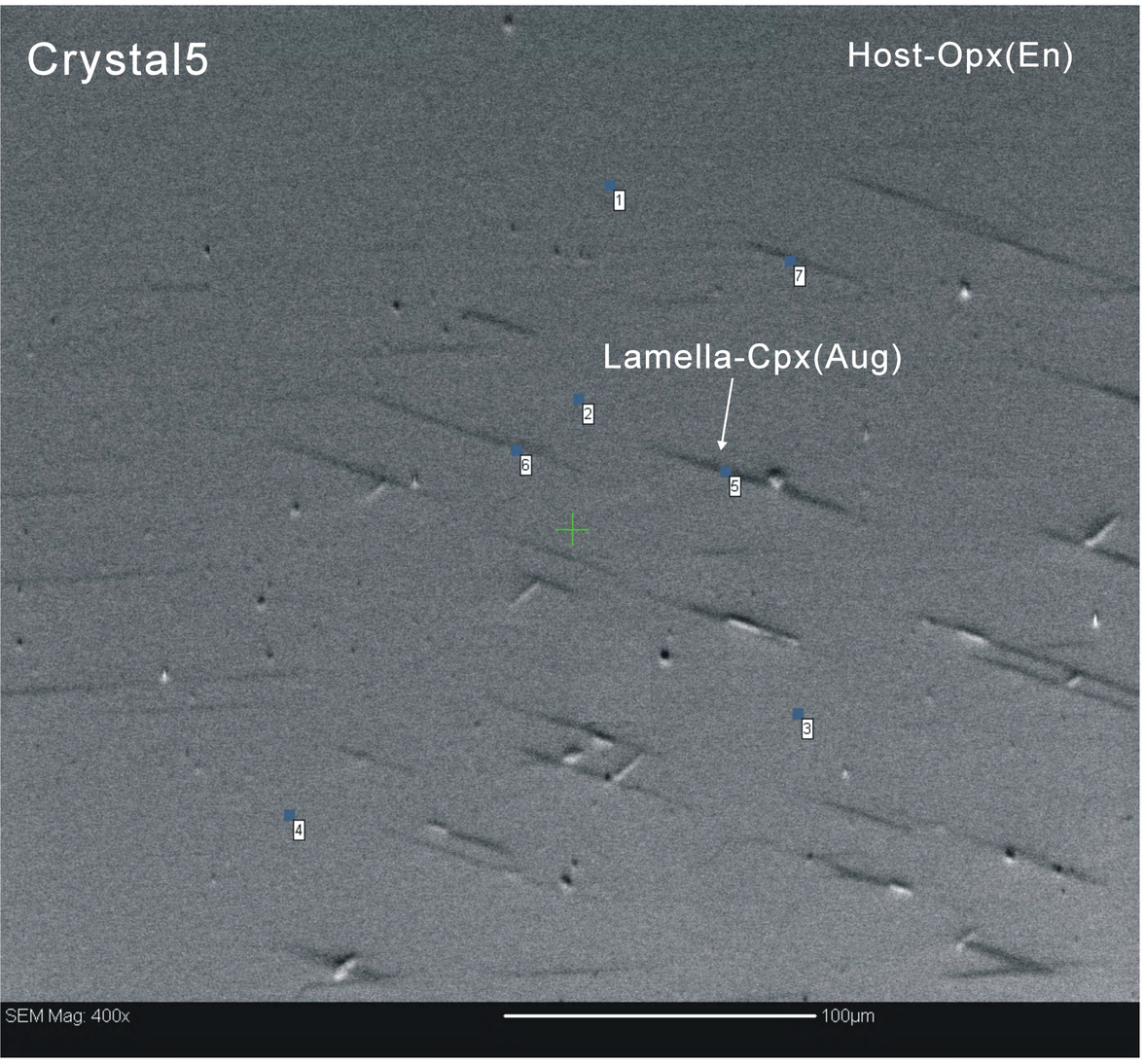
Crystal5
Host-Opx(En)
Lamella-Cpx(Aug)
1
2
3
4
5
6
7
SEM Mag: 400x
100μm

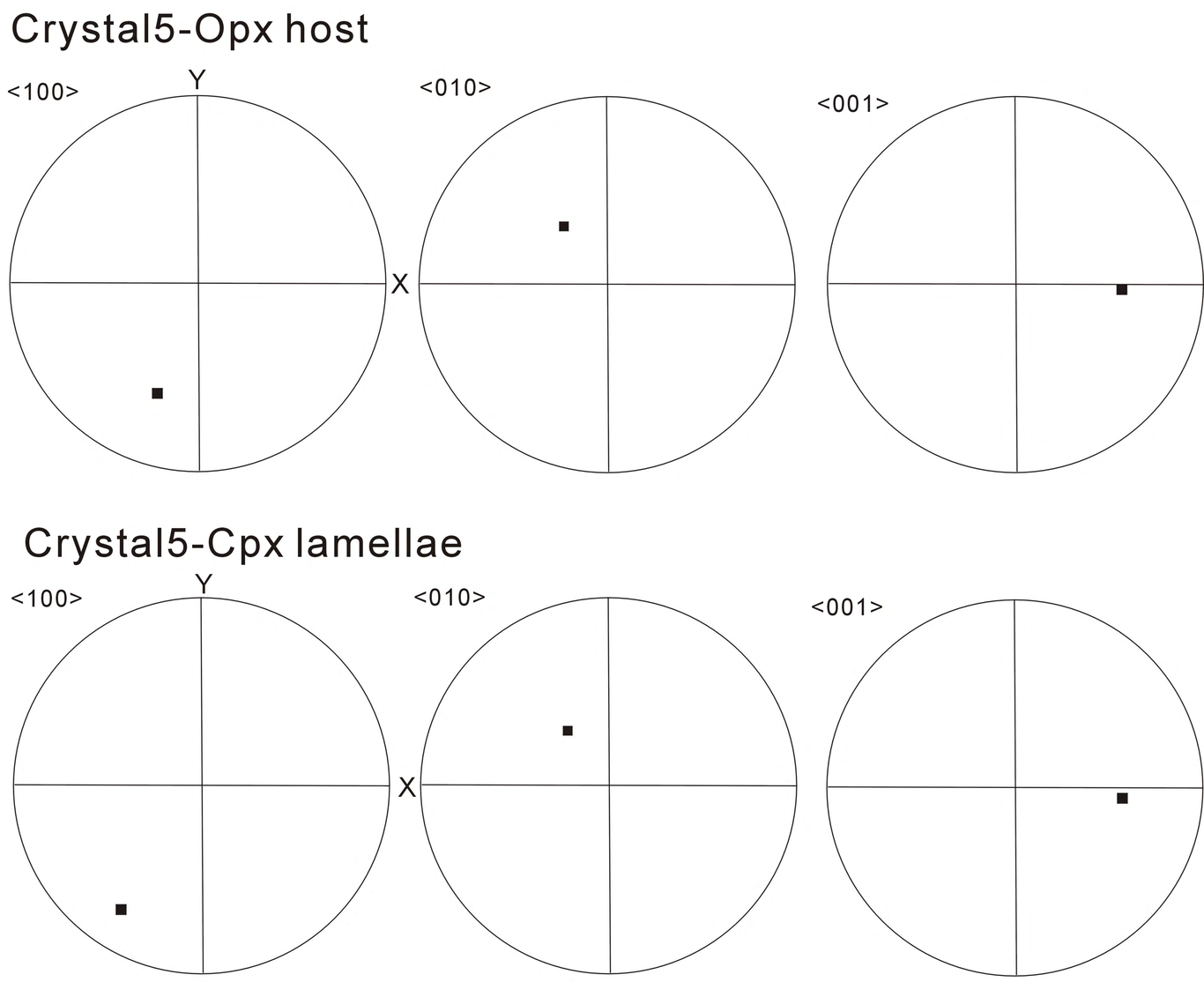
Crystal5-Opx host
<100>
Y
X
<010>
<001>
Crystal5-Cpx lamellae
<100>
Y
X
<010>
<001>

(a)

(b)

Figure 2

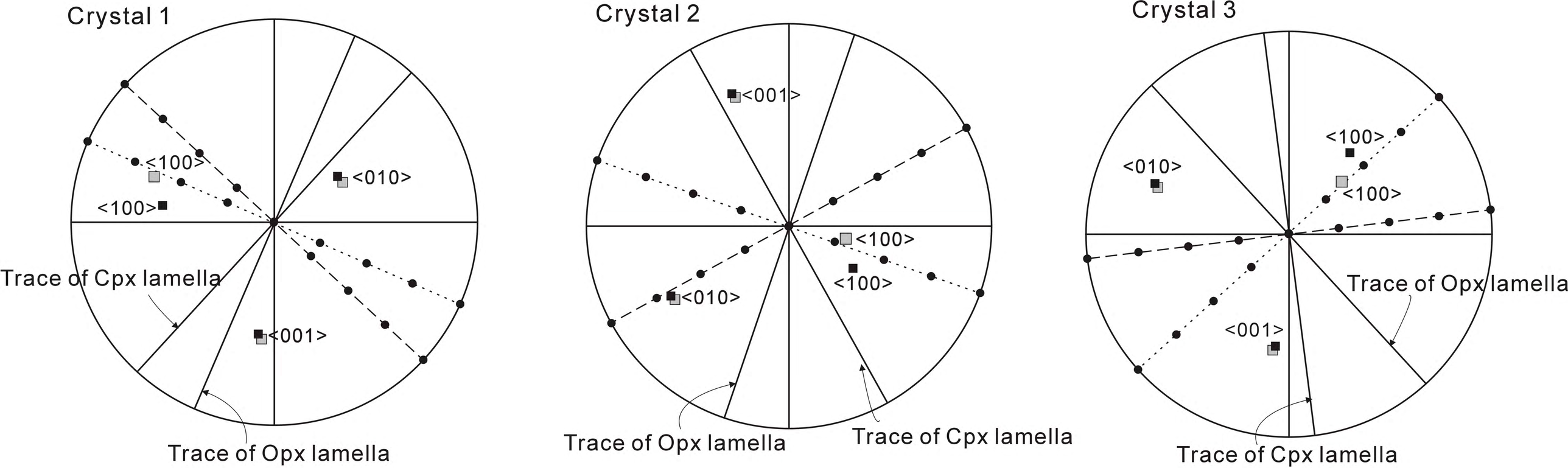
Crystal 1
<100>
<100>
<010>
<001>
Trace of Cpx lamella
Trace of Opx lamella
Crystal 2
<001>
<100>
<100>
<010>
Trace of Opx lamella
Trace of Cpx lamella
Crystal 3
<100>
<010>
<100>
Trace of Opx lamella
<001>
Trace of Cpx lamella
The zone containning Opx lamella
The zone containning Cpx lamella
The pole of the Cpx host
The pole of the Opx lamellae

Figure 3

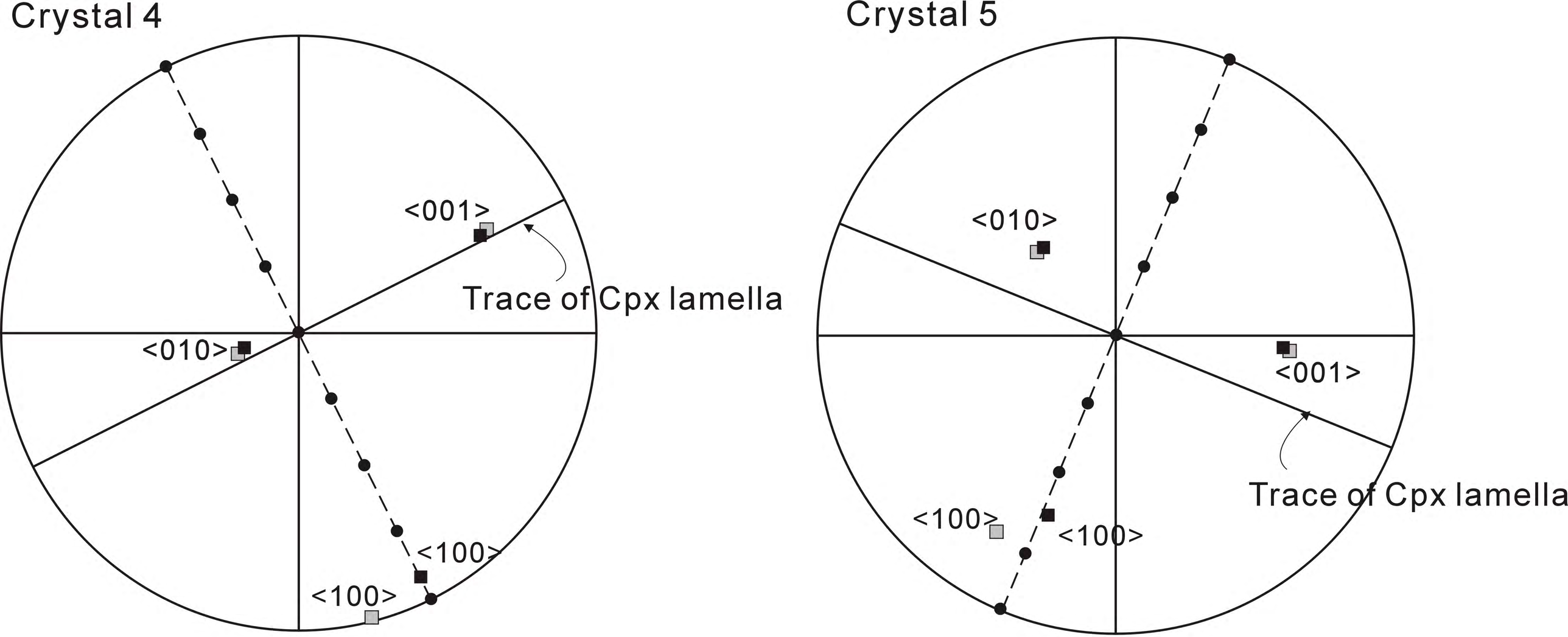
Crystal 4
<001>
Trace of Cpx lamella
<010>
<100>
<100>
Crystal 5
<010>
<001>
Trace of Cpx lamella
<100>
<100>
The zone containning Cpx lamella
The pole of the Opx host
The pole of the Cpx lamellae

Figure 4

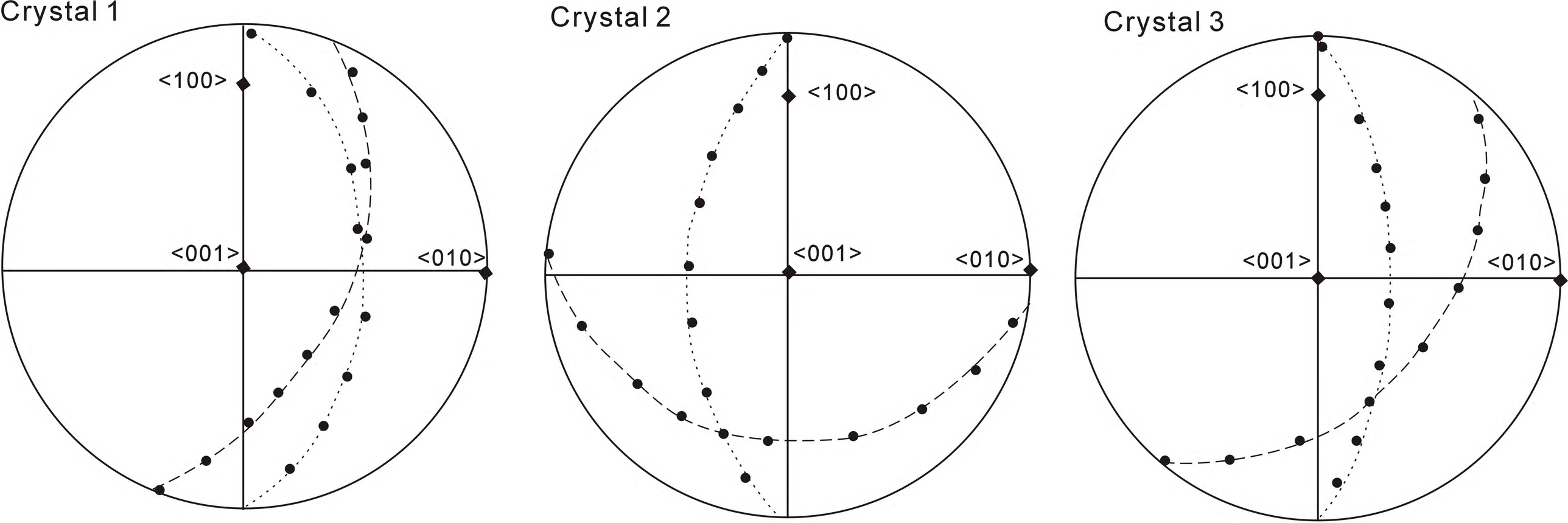
Crystal 1
<100>
<001>
<010>
Crystal 2
<100>
<001>
<010>
Crystal 3
<100>
<001>
<010>
The zone containning Opx lamella
The zone containning Cpx lamella
The pole of the Cpx host

Figure 5

Crystal 4

<001>

<010>

<100>

Crystal 5

<001>

<010>

<100>

Figure 6

The zone containning Cpx lamella

The pole of the Opx host

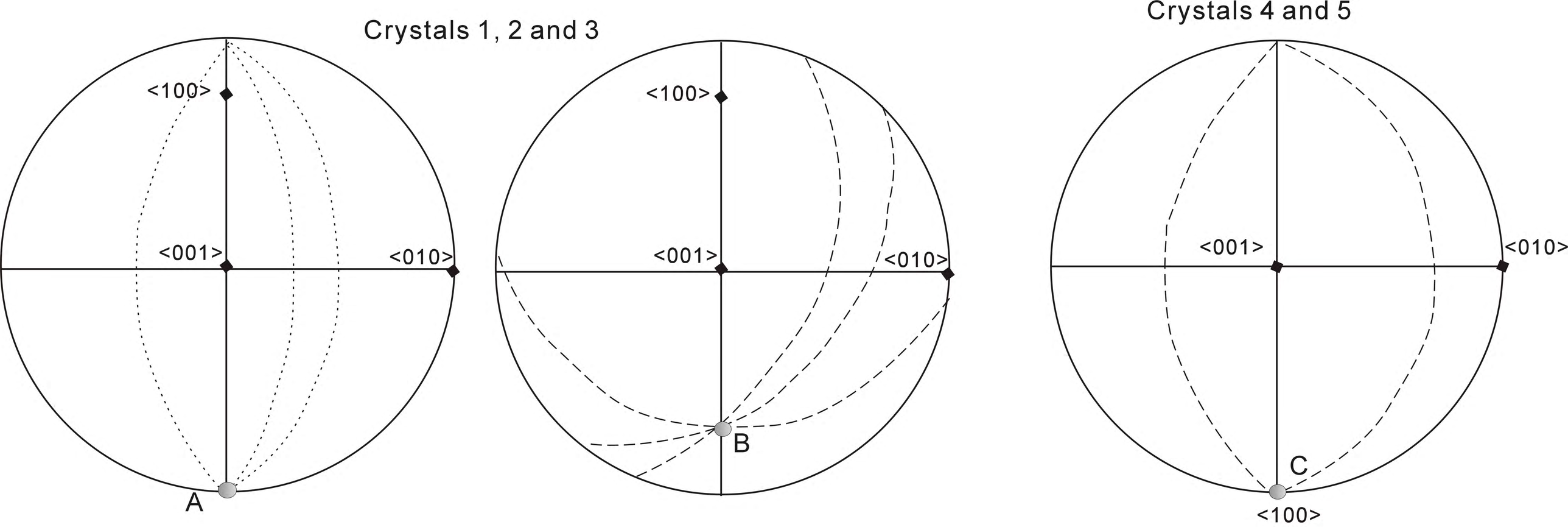
Crystals 1, 2 and 3
<100>
<001>
<010>
A
<100>
<001>
<010>
B
Crystals 4 and 5
<001>
<010>
C
<100>

Figure 7

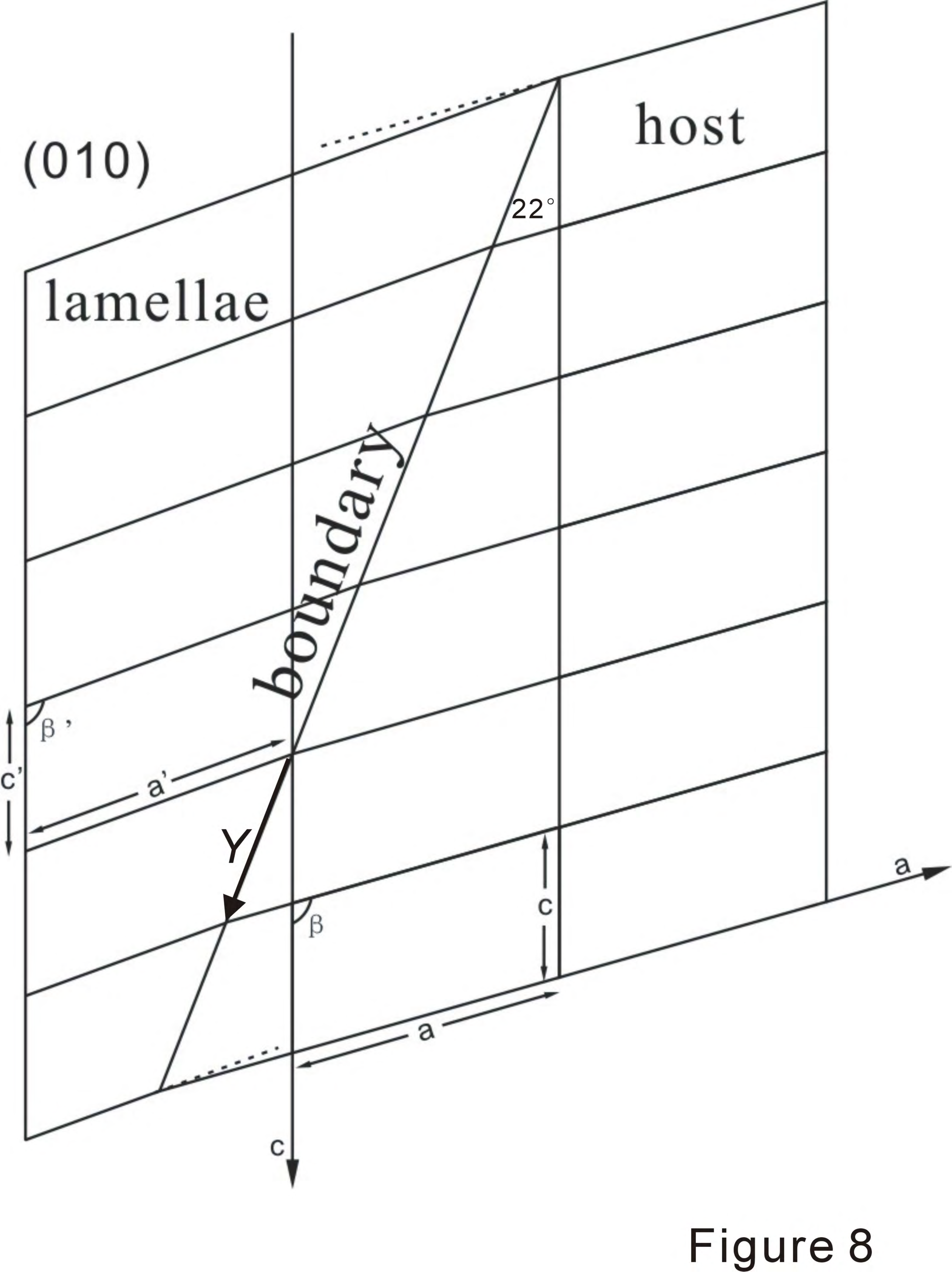

Figure 8

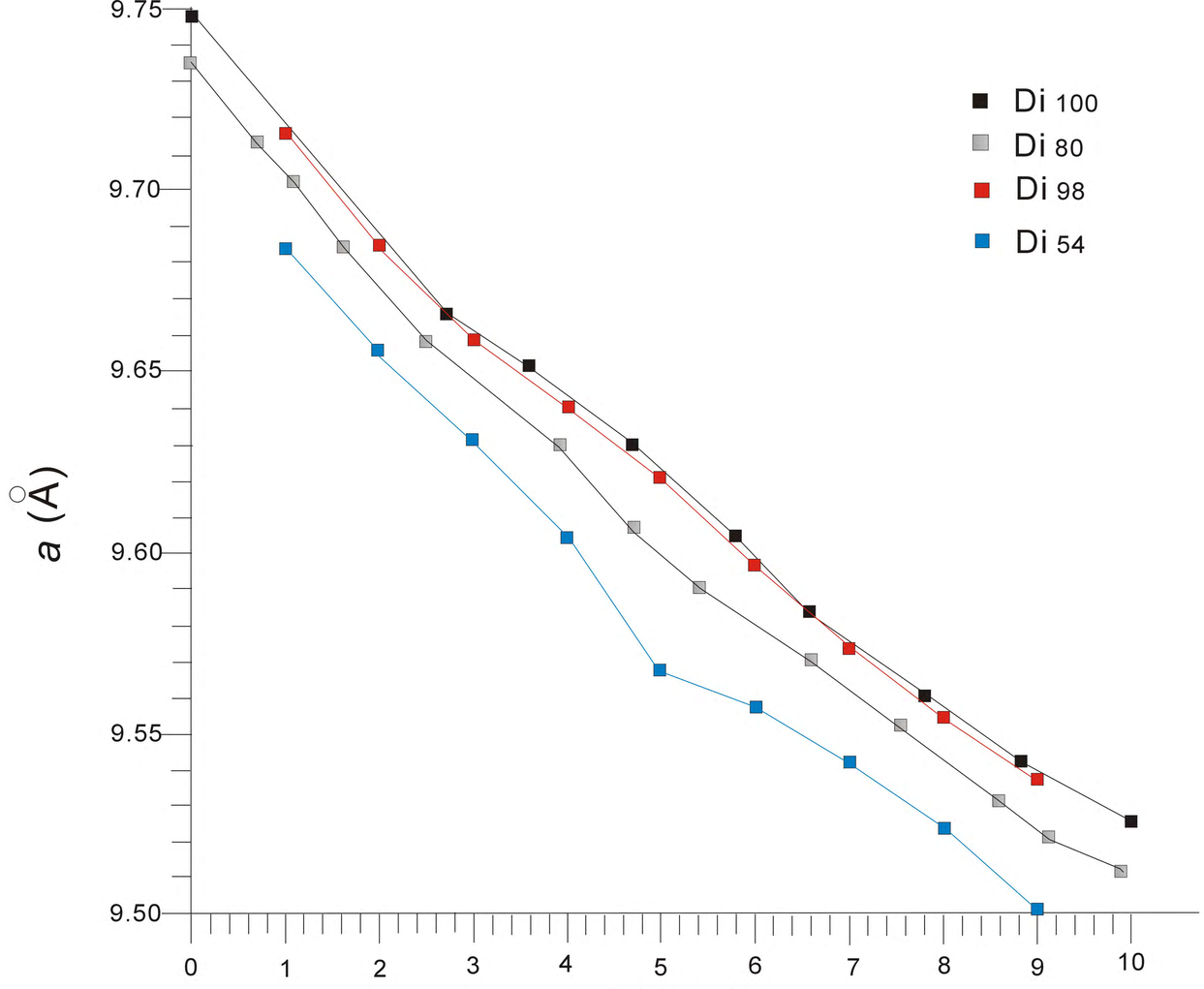
a (Å)
9.75
9.70
9.65
9.60
9.55
9.50
0
1
2
3
4
5
6
7
8
9
10
P(Gpa)
Di 100
Di 80
Di 98
Di 54

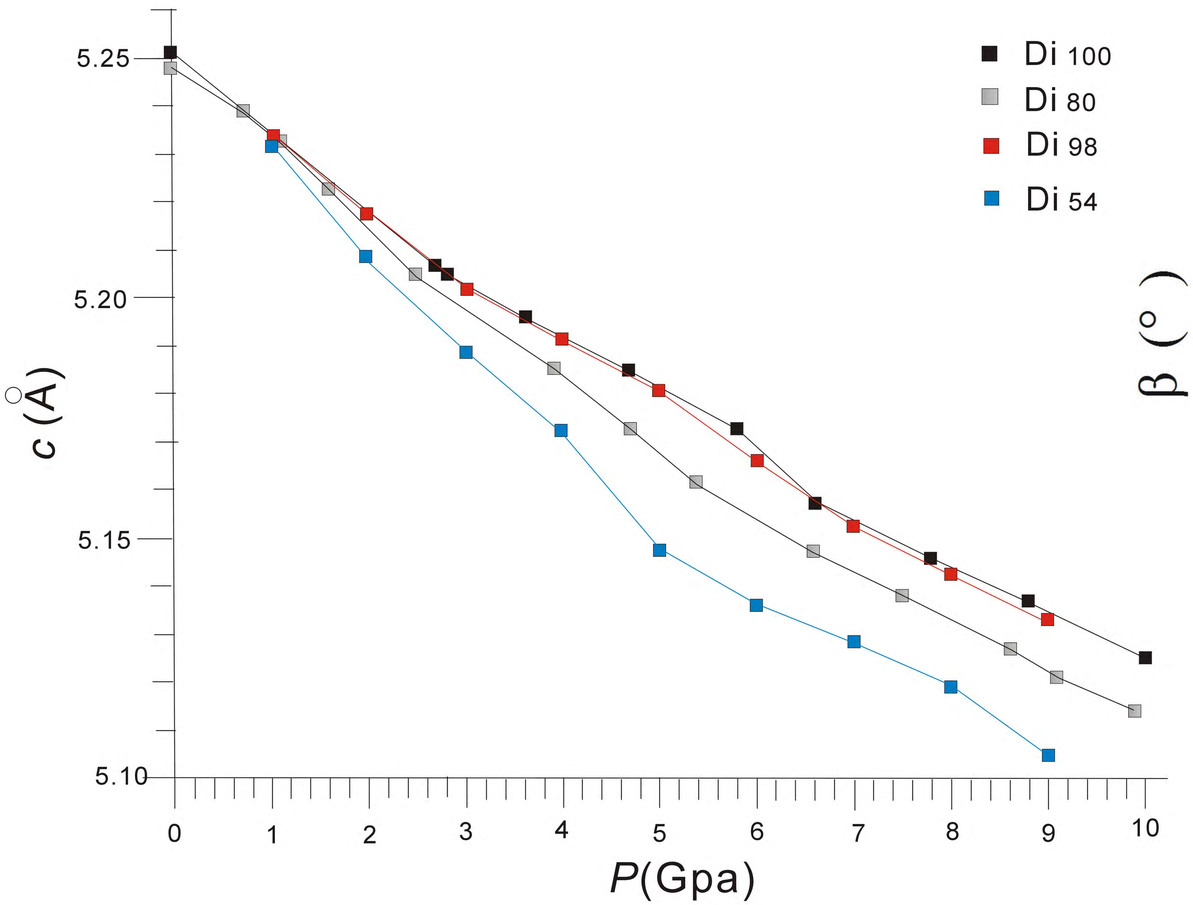
c (Å)
5.25
5.20
5.15
5.10
0
1
2
3
4
5
6
7
8
9
10
P(Gpa)
Di 100
Di 80
Di 98
Di 54

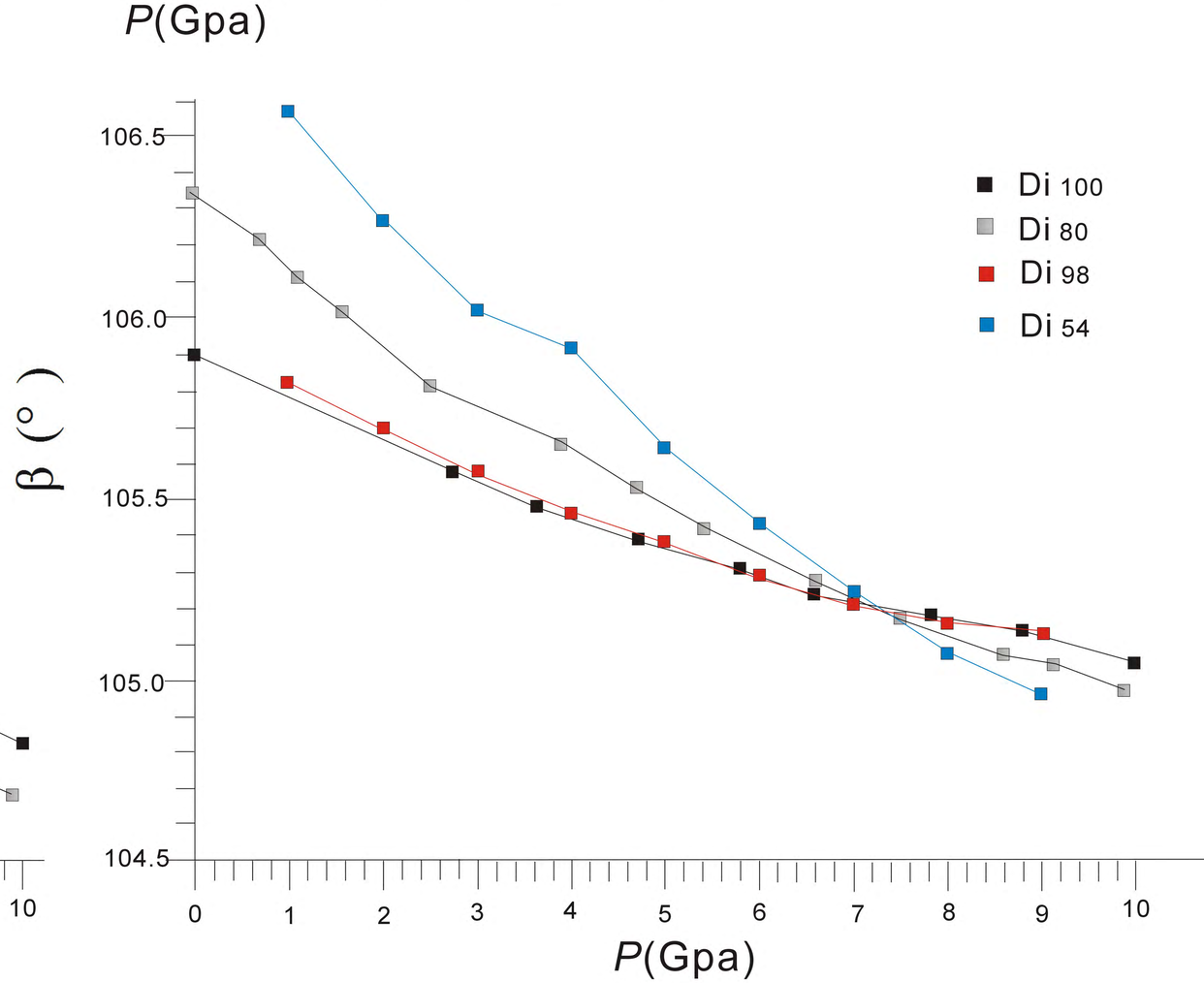
β (°)
106.5
106.0
105.5
105.0
104.5
0
1
2
3
4
5
6
7
8
9
10
P(Gpa)
Di 100
Di 80
Di 98
Di 54

Figure 9